J. Fluid Mech. (2013), *vol.* 735, *pp.* 381–426.
doi:10.1017/jfm.2013.501

Turbulent structure of high-amplitude pressure peaks within the turbulent boundary layer

S. Ghaemi† and F. Scarano

Department of Aerodynamics, Delft University of Technology, Kluyverweg 1, 2629 HS, Delft, The Netherlands

(Received 22 December 2012; revised 5 August 2013; accepted 16 September 2013)

The positive and negative high-amplitude pressure peaks (HAPP) are investigated in a turbulent boundary layer at $Re_\theta = 1900$ in order to identify their turbulent structure. The three-dimensional velocity field is measured within the inner layer of the turbulent boundary layer using tomographic particle image velocimetry (tomo-PIV). The measurements are performed at an acquisition frequency of 10 000 Hz and over a volume of $418 \times 149 \times 621$ wall units in the streamwise, wall-normal and spanwise directions, respectively. The time-resolved velocity fields are applied to obtain the material derivative using the Lagrangian method followed by integration of the Poisson pressure equation to obtain the three-dimensional unsteady pressure field. The simultaneous volumetric velocity, acceleration, and pressure data are conditionally sampled based on local maxima and minima of wall pressure to analyse the three-dimensional turbulent structure of the HAPPs. Analysis has associated the positive HAPPs to the shear layer structures formed by an upstream sweep of high-speed flow opposing a downstream ejection event. The sweep event is initiated in the outer layer while the ejection of near-wall fluid is formed by the hairpin category of vortices. The shear layers were observed to be asymmetric in the instantaneous visualizations of the velocity and acceleration fields. The asymmetric pattern originates from the spanwise component of temporal acceleration of the ejection event downstream of the shear layer. The analysis also demonstrated a significant contribution of the pressure transport term to the budget of the turbulent kinetic energy in the shear layers. Investigation of the conditional averages and the orientation of the vortices showed that the negative HAPPs are linked to both the spanwise and quasi-streamwise vortices of the turbulent boundary layer. The quasi-streamwise vortices can be associated with the hairpin category of vortices or the isolated quasi-streamwise vortices of the inner layer. A bi-directional analysis of the link between the HAPPs and the hairpin paradigm is also conducted by conditionally averaging the pressure field based on the detection of hairpin vortices using strong ejection events. The results demonstrated positive pressure in the shear layer region of the hairpin model and negative pressure overlapping with the vortex core.

Key words: boundary layer structure, turbulent boundary layers

† Present address: Department of Mechanical Engineering, University of Alberta, Edmonton, Alberta, T6G 2G8, Canada. Email address for correspondence: ghaemi@ualberta.ca

1. Introduction

The unsteady pressure field within the turbulent boundary layer is a major source of noise and vibration in transportation vehicles and industrial equipment. Part of the aircraft noise during the landing phase is associated with the acoustic scattering of the pressure fluctuations of the turbulent boundary layer at the trailing edge of wing and high-lift devices (Ffowcs Williams & Hall 1970; Brouwer & Rienstra 2008). The pressure fluctuations within the turbulent boundary layer also cause the cabin noise of aircraft and high-speed trains and structural vibration of pipelines (Clinch 1969; Howe 1991; Willmarth 1975). Apart from the practical aspects, the pressure field is important for development of turbulence models of the pressure–strain term in the Reynolds-averaged Navier–Stokes equation (Kim 1989). The relation of the kinematics of the turbulent boundary layer and the unsteady pressure field and in particular the relation between the flux of vorticity and pressure gradient at the wall is important for flow control applications (Andreopoulos & Agui 1996). As a result, the physical aspects of the pressure field and control strategies for the reduction of the pressure fluctuations (e.g. Rathnasingham & Breuer 2003) have been investigated by researchers.

The broad range of pressure fluctuations within the turbulent boundary layer was initially classified into low- and high-frequency fluctuations by Willmarth & Wooldridge (1962). They conducted a comparison and associated the low-frequency fluctuations with a high advection velocity using space–time correlation of wall pressure. Later, Bull (1967) assumed a one-to-one relation between the wall-pressure fluctuations and the turbulent sources and estimated an advection velocity of $0.8U_\infty$ for the low-frequency and $0.5U_\infty$ for the high-frequency pressure fluctuations (U_∞ is the free-stream velocity). Bull (1967) and other researchers also located the low-frequency pressure fluctuations at $(0.25–0.3)\delta$ (δ is the boundary layer thickness) and the high-frequency structures in the buffer layer by projecting the advection velocity on the mean velocity profile. Farabee & Casarella (1991) revisited the classification by applying scaling parameters of streamwise cross-spectra and confirmed the correspondence of the high- and low-frequency content to the turbulent sources in the inner and outer regions, respectively. The lack of access to the internal pressure field in the experimental studies was a limiting factor which motivated supplementary investigations using numerical simulation.

Large-eddy simulation of the pressure field within a channel flow by Kim (1983) confirmed the conjectures of the previous experiments regarding the location of the low-frequency pressure fluctuations. Kim (1989) used direct numerical simulation (DNS) of a turbulent channel flow to resolve the debate of previous theoretical works over the contribution of the rapid (linear) and slow (nonlinear) terms of the Poisson equation (Corcos 1963; Willmarth 1975). Results showed that the slow term dominates throughout the channel except in the vicinity of the wall where both terms become comparable. Chang, Piomelli & Blake (1999) further investigated the relation between the source terms of the velocity field and the wall pressure from a DNS database. They observed significant contribution of the viscous layer to high wavenumbers, the logarithmic layer to low wavenumbers, and the dual contribution of the buffer layer to both low- and high-wavenumber pressure fluctuations. Estimating the wall-normal location of pressure sources and conjecturing their turbulent structure was the most common method of experimental and numerical investigations. However, in a turbulent boundary layer, there are several types of coherent structures at any wall-normal distance which necessitates a more detailed analysis to characterize the turbulent structure of different pressure fluctuations.

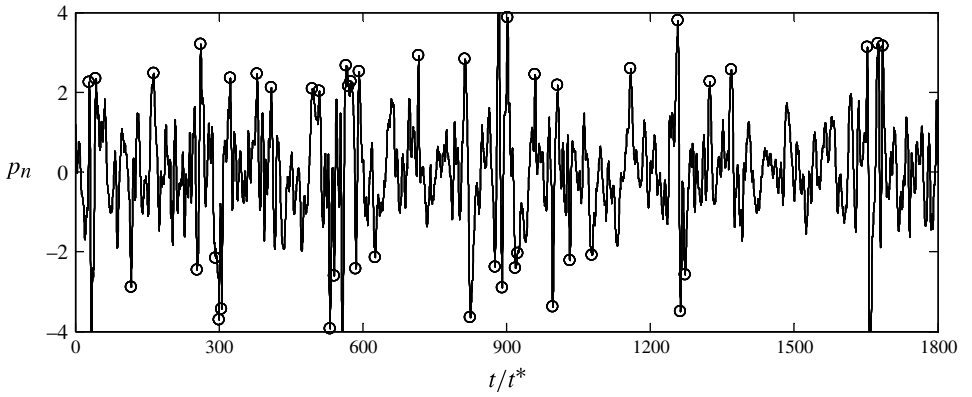

FIGURE 1. Wall-pressure signal of a turbulent boundary layer at $Re_\theta = 1900$ (Reynolds number based on the momentum thickness) measured using an electret condenser microphone. High-amplitude peaks of $p_n = |p/p_{rms}| > 2$ are indicted using an 'o' symbol.

Identification of the turbulent structure of a non-local property such as pressure is not straightforward since it depends on the flow field over a large domain. This complexity has been augmented by the limitation of the traditional experimental techniques to point-wise measurement of velocity and wall pressure. Kobashi & Ichijo (1986) averaged hot-wire velocity measurements conditioned on wall-pressure frequency and argued that the high-frequency pressure fluctuations of the buffer layer are related to burst events and the low-frequency pressure fluctuations are related to the large-scale vortices interacting with the mean shear flow. Using a large-eddy simulation database, Kim (1983) identified the ejection process at the end of the sweeping motion as the source of localized adverse pressure events. Later, Kim (1989) investigated the spatial structure of the pressure sources by scrutinizing the instantaneous pressure field from a DNS database, suggesting further study due to the perplexing observation of no apparent correlation between the spanwise vorticity and the streamwise gradient of pressure. Chang *et al.* (1999) conjectured on the relation of the horseshoe vortices and the pressure sources based on the kinematics of the rapid and slow source terms of the Poisson pressure without any statistical evidence. Naguib, Wark & Juckenhöfel (2001) showed that, in contrast to stochastic estimations of the velocity events, a linear stochastic estimation does not provide a reasonable representation of the pressure events and the quadratic terms should be included. This complexity in source identification is associated with the nonlinearity and the presence of a broad range of pressure fluctuations. However, among this broad range, the high-amplitude pressure peaks (HAPPs) are of particular importance due to their unique features (Schewe 1983).

The HAPPs refer to both the negative and positive pressure fluctuations which exceed a certain threshold typically 2–3 times larger than the r.m.s. of pressure fluctuations (p_{rms}) as illustrated in figure 1. The data of this figure belong to wall-pressure fluctuations beneath a turbulent boundary layer measured using an electret-condenser microphone as detailed in § 2.2. The pressure fluctuations (p) are normalized as $p_n = p/p_{rms}$ and plotted against non-dimensional time which is normalized using the inner time scale (t^*) introduced in § 2.1. The important feature of the HAPPs is their low occurrence frequency and high contribution to the total p_{rms} (Kim 1989). The analysis of the probability density function (p.d.f.) $f(p_n)$ of the

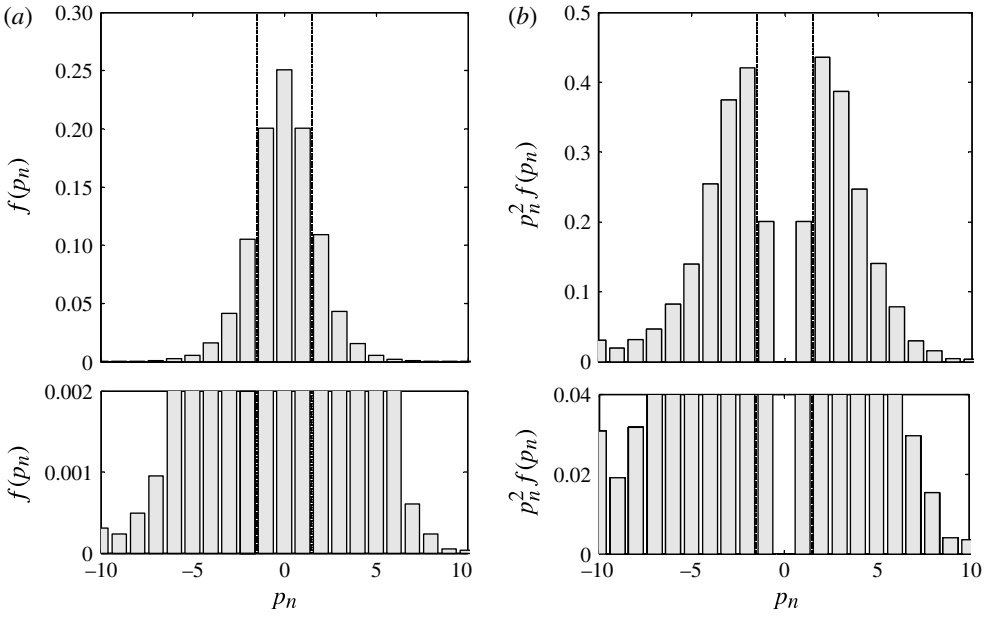

FIGURE 2. (*a*) The p.d.f. of wall pressure $f(p_n)$ and (*b*) the pre-multiplied p.d.f. showing the fractional contribution of the fluctuations to the total mean-square pressure fluctuation (p_{rms}). The lower plots are magnified views.

measured wall-pressure data in figure 2 shows that pressure fluctuations larger than $2p_{rms}$ (both positive and negative) have 13 % occurrence probability while forming 60 % of the total p_{rms} energy. Their low occurrence and high contribution to the p_{rms} makes the high-amplitude peaks of particular interest for flow control applications related to sound generation and structural vibration (Alfredsson, Johansson & Kim 1988*b*). These extreme events are associated with the intermittency of the pressure field as is evident in the high kurtosis (flatness factor, k_p) of the pressure fluctuations ($k_p = 4.9$, Schewe 1983). The characterization of the HAPPs and in particular their turbulent structure has been pursued to understand the intermittent behaviour and also the future development of flow control strategies.

Statistical characterization of the footprint of the HAPPs on the wall surface has been initially conducted by Schewe (1983) who estimated a characteristic frequency of $f^+ = f\nu/u_\tau^2 = 0.52$. Here, f is the reciprocal of the average peak duration (2.3 ms), ν is the kinematic viscosity and u_τ is the friction velocity. Further analysis using the conditional averaging method estimated an advection velocity of $0.53U_\infty$ ($11.9u_\tau$) which puts the HAPPs at a wall distance of $y^+ = 21$ assuming that the source moves with the average velocity profile. Karangelen, Wilczynski & Casarella (1993) also characterized the HAPPs through statistical analysis and conditional averaging of wall pressure. They observed that the occurrence frequency of the HAPPs is close to the burst frequency of the low-speed streaks and supported the conjectures of Haritonidis, Gresko & Breuer (1988) on their association with the burst events. However, the experimental and numerical evidence on the turbulent structure of the HAPPs is limited and contradictory. According to our knowledge the following experimental and numerical investigations have addressed the turbulent structure of the HAPPs in a turbulent boundary layer.

(i) Johansson, Her & Haritonidis (1987) applied simultaneous wall-pressure and hot-wire velocity measurements to investigate the HAPPs. Their conditional averaging based on wall-pressure amplitude and also detection of shear layers from the velocity measurements using the variable-interval time-averaging (VITA) technique showed that the positive HAPPs are associated with the shear layers in the buffer layer. These turbulent structures are also referred to as burst events (Kim, Kline & Reynolds 1971; Johansson & Alfredsson 1982) and exhibit a rapid increase of streamwise velocity fluctuation (u) from a negative value to a positive value along with variation of wall-normal velocity fluctuation (v) from positive to negative (an ejection followed by a sweep event). Johansson *et al.* (1987) also carried out a similar analysis on the negative HAPPs and associated them with sweep-type motions (a peak in u). They suggested that the negative HAPPs occur during the deceleration phase (decreasing u and increasing v) of the sweep event.

(ii) Haritonidis *et al.* (1988) applied conditional averaging to wall-pressure measurement and observed a strong connection between the HAPPs and the wall-normal velocity component. Bidirectional analysis was conducted and averages were obtained based on the detection of HAPPs and also flow events. The conditional averages demonstrated similar trends to those of Johansson *et al.* (1987); however, Haritonidis *et al.* (1988) emphasized more the association of both positive and negative HAPPs with the wall-normal motions (v component).

(iii) Robinson (1991) in his review of coherent motions in the turbulent boundary layer introduced the strong vortices of the turbulent boundary layer as a source of pressure disturbance by virtue of their low-pressure source. However, no evidence was provided to support the association of the negative HAPPs with the vortical structures of the turbulent boundary layer. He also linked the shear layer structures to positive wall-pressure fluctuations based on the investigation of Johansson *et al.* (1987).

(iv) De Ojeda & Wark (1997) conducted simultaneous planar particle image velocimetry (PIV) and wall-pressure measurement using an array of microphones. The positive pressure peaks were associated with the stagnation point of the shear layer structures separating the upstream high-speed flow from the downstream low-speed region. They associated the negative pressure peaks, based on visual inspection of the instantaneous data, with the roll-up motion at the upstream or downstream location of the positive pressure peaks.

(v) Kim, Choi & Sung (2002) scrutinized the source of the HAPPs from a DNS database of turbulent boundary layers by conditional averaging of streamwise vorticity and also the quadrant analysis of the velocity fluctuations based on detection of positive and negative HAPPs. They argued that the positive HAPPs are related to inward motions (sweep) and the negative peaks to outward motion (ejection) while both events are produced by a counter-rotating pair of upstream quasi-streamwise vortices within the buffer layer.

The discrepancies among the above investigations could be due to the phase jitter in the conditional averaging of Johansson *et al.* (1987) and Haritonidis *et al.* (1988) or because Kim *et al.* (2002) limited their investigation of the conditional averaging to streamwise vorticity at an upstream location of the pressure peak. The contradictory results require further investigation in order to characterize the structure of the HAPPs in the turbulent boundary layer and this is the subject of the current investigation.

The experiments on the pressure field within a turbulent boundary layer are not as comprehensive as the studies of the velocity field, mainly due to the lack of a

robust pressure measurement technique (Tsuji *et al.* 2007). The previous experiments on turbulent boundary layer have been obliged to use miniaturized pressure transducers (Willmarth & Wooldridge 1962; Bull 1967) or condenser microphones (Blake 1970) which are intrusive and provide point-wise diagnostics. The shortcomings can be addressed by the recent advances in the PIV technique in combination with the Poisson pressure equation. The velocity field measured by the PIV technique was first applied by Baur & Köngeter (1999) and Gurka *et al.* (1999) to obtain the unsteady pressure field through integration of the Poisson pressure equation. In the last decade, the method has been applied to more complicated flows with the improvements in the PIV technique. Liu & Katz (2006) applied a four-exposure PIV system to evaluate the material derivative using the Lagrangian method followed by an omni-directional algorithm for the integration of the pressure gradient. Violato, Moore & Scarano (2011) extended the Lagrangian evaluation of the material derivative to three-dimensional particle trajectories using tomo-PIV. Charonko *et al.* (2010) assessed the effect of different factors such as the integration method, grid resolution and sampling rate on the evaluation of the pressure field. Koschatzky *et al.* (2011) used time-resolved planar PIV to obtain the pressure field in a cavity flow. De Kat & van Oudheusden (2012) determined the pressure field around a square cylinder and evaluated the results against surface pressure measurement using transducers. In a recent study, time-resolved three-dimensional velocity measurement by a high-speed tomo-PIV technique was applied to obtain the pressure field within the turbulent boundary layer by Ghaemi, Ragni & Scarano (2012). The obtained pressure field was also compared to surface pressure measurements using electret condenser microphones.

In the current investigation, the three-dimensional velocity measurement of a time-resolved tomo-PIV system is applied to obtain the unsteady pressure fields within the inner layer of a turbulent boundary layer. The obtained simultaneous velocity and pressure fields are applied to investigate the turbulent structure of both the positive and negative HAPPs. Instantaneous visualization of the HAPPs and conditional averaging of three-dimensional velocity and pressure fields are applied in the investigations.

2. Experimental procedure

2.1. *Flow setup*

The experiments were performed in a low-noise (maximum of 50 dB) open-test-section vertical wind tunnel with a circular cross-section of 0.6 m in diameter and a turbulence intensity of 0.02 % at free-stream velocity of 10 m s^{-1}. The turbulent boundary layer is generated over a flat plate of 2 m length at zero angle of attack with an elliptical leading edge and a sharp symmetric trailing edge as shown in figure 3. The plate spanned the entire test section and spanwise-uniform laminar-to-turbulent transition of the boundary layer is forced at 250 mm downstream of the leading edge using a 20 mm strip of sparsely spread 0.8 mm carborundum particles on both sides of the plate. The flat plate is made of chipboard except the measurement region, located 1.5 m downstream of the leading edge, which is made of aluminium to provide a smooth surface along with precise installation of the microphones.

The boundary layer parameters are summarized in table 1 and are obtained using 2C-PIV recordings processed by the ensemble-of-correlations technique as detailed in § 2.3. The uncertainty in average velocity from this technique is estimated to be about ±1 %. The measured free-stream velocity and the boundary layer thickness are $U_\infty = 9.0$ m s^{-1} and $\delta_{99} = 29.9$ mm, respectively. The Reynolds number Re based on δ_{99} (δ) and U_∞ is $Re_\delta = 18\,400$, that based on θ (momentum thickness) and U_∞

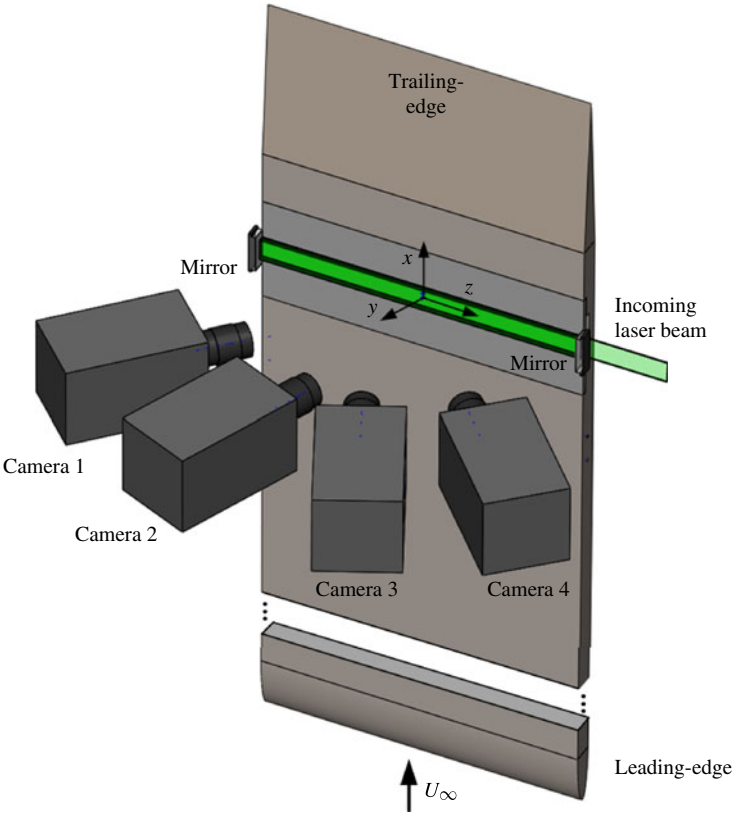

FIGURE 3. (Colour online) The experimental setup of the tomo-PIV system illustrating the arrangement of the cameras and the multi-pass light amplification with respect to the vertically mounted flat plate.

Parameter	Units	
U_∞	m s^{-1}	9.0
δ_{99}	mm	29.9
θ	mm	3.1
$Re_{\delta 99}$		18 400
Re_θ		1900
Re_τ		770
u_τ	m s^{-1}	0.38
λ	μm	39
H		1.33
t^*	μs	102

TABLE 1. Boundary layer parameters in the measurement region located 1.5 m downstream of the leading edge.

is $Re_\theta = 1900$, and that based on δ and u_τ (friction velocity) is $Re_\tau = 770$. The inner variables are $u_\tau = 0.38$ m s^{-1} and the wall unit $\lambda = 39$ μm, which are obtained from the slope of the measured velocity profile in the sublayer region with about ±5 %

uncertainty. The shape factor is $H = 1.33$ confirming a fully developed turbulent boundary layer. The time scale $t^* = \nu/u_\tau^2 (=102\ \mu s)$ is used to obtain non-dimensional frequency $f^+ = t^* f$ and vorticity $\omega^+ = t^* \omega$. The averaged velocity in the streamwise (X), wall-normal (Y) and spanwise (Z) directions is indicated by U, V and W (components of the velocity vector $\boldsymbol{U}$), respectively. The fluctuating velocities are specified by lower-case letters u, v, and w, and the vorticity components by ω_x, ω_y and ω_z in X, Y, and Z, respectively.

2.2. *Wall-pressure measurement*

The pressure fluctuations at the wall have been measured using an electret condenser Sonion 8010T microphone to further validate the pressure field obtained from the tomo-PIV measurement. This instrument measures from 10 to 20 000 Hz while it has a constant sensitivity of -33.5 dB (21 mV Pa^{-1}) from 250 to 7500 Hz. The maximum noise level in this frequency range is 28 dB which is equivalent to an r.m.s. pressure fluctuation of 0.5 mPa. The phase shift is also negligible ($\pm 5°$) in the range of 250–7500 Hz as the corresponding amplitude response is flat. The signal is conditioned using a first-order low-pass analogue filter starting at 10.6 kHz and is followed by an amplifier. The signal is sampled at 50 kHz using a National Instrument NI-9215 data acquisition system with 16 bits resolution placed in an NI cDAQ-9172 chassis.

The microphone is placed behind a pinhole orifice of $d = 0.2$ mm (5λ) diameter to prevent attenuation of small-scale pressure fluctuations, which satisfies the 20λ maximum pinhole size suggested by Lueptow (1995) and Tsuji *et al.* (2007). The orifice aspect ratio (length/diameter) is 2.5, which is slightly higher than the lower limit suggested by Shaw (1960). This pinhole orifice induces a resonant frequency of $\sim$14 kHz which is higher than the cut-off frequency of the analogue filter (10.6 kHz). Further assessment of the system of installed microphones and the pinhole orifices relative to a reference microphone is available in Ghaemi *et al.* (2012) confirming that the influence of the Helmholtz resonance is negligible up to 5 kHz and further correction of amplitude or phase due to the resonance is not required up to this limit. Therefore, the maximum reliable temporal resolution of the microphone system is limited to 5 kHz. In addition, the amplitude was calibrated to account for the applied analogue signal amplification using a known sound wave (250 Hz) generated by a piston-phone (G.R.A.S. Type 42AA) instrument equipped with an artificial mouth.

2.3. *Planar PIV*

The planar PIV system is applied here for characterization of the inner and outer parameters of the boundary layer due to its higher spatial resolution and lower processing time in comparison to the tomo-PIV system. The illumination is provided by a diode pumped dual-cavity Nd:YLF laser (Litron Lasers, LDY303HE) with each cavity delivering a pulse energy of 22.5 mJ pulse^{-1} at 1 kHz operation frequency (527 nm wavelength). The laser beam diameter is 3 mm at the output of the laser head and is shaped into a laser sheet of approximately 1 mm thickness and 60 mm width by a combination of spherical and cylindrical lenses. A Photron Fast CAM SA1 camera with a 12-bit CMOS sensor of 1024×1024 pixels (pixel pitch 20 μm) equipped with a Nikon objective of 105 mm focal length set to aperture of $f/4$ is used to record the light scattered by the illuminated tracers. The plane of focus is slightly offset with respect to the illumination plane (defocusing) generating a blurred spot spanning approximately 2 pixels to mitigate the bias errors associated with pixel-locking (Westerweel 1997). The test section is globally seeded using 1 μm

Repetition rate	200 Hz
FOV ($X \times Y$)	118×1024 px^2 6.95 mm $\times$ 60.3 mm $0.23\delta \times 2.02\delta$ $178\lambda \times 1546\lambda$
Digital resolution (S)	17.0 px mm^{-1}
Magnification (M)	0.34
Number of samples	4200
Interrogation method	Ensemble of correlations
IA	8×8 px^2 0.47 mm $\times$ 0.47 mm $12\lambda \times 12\lambda$
IA overlap	75 %
Vectors per field	59×512

TABLE 2. System parameters of the planar PIV system.

droplets generated with a SAFEX smoke generator dispersing particles upstream of the wind-tunnel settling chamber.

Planar measurements were conducted in the XY-plane over a field of view (FOV) of 6.95 mm $\times$ 60.31 mm ($X \times Y$). The boundary layer mean velocity profile and the turbulent fluctuations were characterized by measurements conducted at 200 Hz using a cropped CMOS sensor (118×1024 pixels). A set of 4200 double-frame recordings with 100 μs pulse separation was acquired during 21 s. The recordings were analysed using DaVis 8.0 (LaVision) with ensemble averaging of correlation maps for the mean velocity distribution (Meinhart, Wereley & Santiago 2000). The ensemble cross-correlation technique allows the use of interrogation areas (IA) as small as 8×8 pixels (0.47 mm $\times$ 0.47 mm) with 75 % overlap yielding a vector spacing of 118 μm. Table 2 shows the system parameters for the 2C-PIV system.

2.4. *Time-resolved tomo-PIV*

The tomo-PIV system is applied to measure the time-resolved evolution of the three-dimensional velocity field within the inner layer of the turbulent boundary layer. The three-dimensional and time-resolved features of the technique are essential in evaluating the pressure field, which is discussed in the next section. The measurement volume has been optimized to only cover the inner layer, which is speculated to contain the sources of the high-amplitude pressure peaks. The investigation of Schewe (1983) estimated the locus of the high-amplitude peaks to be at $Y^+ = 21$ based on projection of their advection velocity on the mean velocity profile. Johansson *et al.* (1987) demonstrated that the turbulent structures causing the high-amplitude peaks extend up to $Y^+ = 185$ based on shear layer detection. The numerical study of Kim *et al.* (2002) also confirms that the high-amplitude wall-pressure peaks are linked to the turbulent structures within the inner layer. As a result the measurement volume of the current tomo-PIV experiment is chosen to cover the inner layer from the wall surface up to $Y^+ = 149$.

The tomo-PIV technique uses simultaneous image acquisition from cameras at different viewing angles to reconstruct a volumetric distribution of the particles within the illuminated volume. This is followed by three-dimensional cross-correlation of successive volumetric particle reconstructions to obtain the three velocity components (Elsinga 2008). The initial laser beam emitted from the same Nd-YLF laser as for the planar PIV experiment is collimated into a laser sheet of 20 mm width

(along X) and 1.5 mm thickness (along Y) that enters a multi-pass light amplification system consisting of two mirrors on the spanwise side of the flat plate as shown in figure 3. The multi-pass system of this work applies successive passes of a collimated laser sheet along the Z-direction while it progresses in the Y-direction, forming an illuminated volume with a cross-section of 16.3 mm $\times$ 5.8 mm along the span of the flat plate. This configuration provides a more homogeneous light distribution in the X-direction in comparison to the configuration applied by Schröder *et al.* (2008) and Ghaemi & Scarano (2010) that is based on multiple reflections of a beam with circular cross-section. The imaging system consists of four Photron Fast CAM cameras equipped with Scheimpflug adapters and 105 mm Nikon objectives positioned in a YZ-plane. The inner cameras (number 2 and 3) have aperture setting of $f/5.6$ and an angle of $\pm 15^\circ$ and the two outer cameras (number 1 and 4) have aperture setting of $f/8$ and an angle of $\pm 30^\circ$ with respect to the XY-plane. The illuminated volume has been seeded with 1 μm droplets at a concentration of approximately 4 particles mm^{-3} resulting in a particle image number density of approximately 0.08 particles per pixel (p.p.p.). A set of 14 000 single-frame recordings was acquired at 10 kHz acquisition rate with pulse separation of 100 μs.

The mapping function of the tomographic system is obtained by calibration using a two-layer target. The residual system pointing accuracy is monitored with the volume-self-calibration technique (Wieneke 2008) and the r.m.s. of disparity is reduced to less than 0.03 pixels in the entire domain. Minimum intensity subtraction was followed by subtraction of a local neighbourhood minimum for background light elimination. The image intensity was normalized by the average over a kernel of 51 pixels. The three-dimensional object reconstruction is obtained with iterative application of the multiplicative algebraic reconstruction technique (MART, Herman & Lent 1976) performed on a 48-core PC using the LaVision software Davis 8.0. The cross-correlation is performed with multi-grid iterative volume deformation (VODIM, Scarano & Poelma 2009) implementing the correlation sliding-average technique over three successive correlation maps as detailed in Ghaemi *et al.* (2012). This method enhances the signal-to-noise ratio, especially in low particle displacement regions near the wall. However, the averaging procedure also reduces the temporal resolution of the system to 300 μs equivalent to 3.33 kHz. This temporal sampling rate theoretically resolves fluctuations up to 1.67 kHz according to the Nyquist criterion. The calculation is accelerated using the preceding vector field (100 μs earlier) as the initial predictor. Interrogation volumes (IV) of 32 $\times$ 16 $\times$ 32 voxels (1.68 mm $\times$ 0.84 mm $\times$ 1.68 mm) in $X \times Y \times Z$ with 75 % overlap have been used that contain on average nine particles. The no-slip condition is applied at the wall to stabilize the calculation of the velocity close to the surface (Theunissen, Scarano & Reithmuller 2008). The stretching of the interrogation volumes in the direction of minimum velocity gradient allows an increase of the spatial resolution in regions with strong gradients and vortical structures. Novara, Ianiro & Scarano (2013) investigated the effect of non-cubic interrogation windows and demonstrated measurement improvement in terms of vorticity peaks and spatial resolution. The system parameters associated with the tomo-PIV are summarized in table 3.

The random error of the tomo-PIV system is expected to be $\sim$0.15 voxels for a double-pulse configuration according to Scarano & Poelma (2009). However, Ghaemi *et al.* (2012) observed that the application of a sliding-average correlation to single-frame time-resolved PIV reduces the random error noise. The random error noise of the current tomo-PIV experiment is estimated to be about $\varepsilon_{u,rand} = 0.1$ voxels (0.05 m s^{-1}) based on the velocity power spectrum, which will be discussed in § 3.

Repetition rate	10 000 Hz
Reconstructed volume ($X \times Y \times Z$)	$310 \times 110 \times 460$ voxels 16.3 mm × 5.8 mm × 24.2 mm $0.55\delta \times 0.19\delta \times 0.81\delta$ $418\lambda \times 149\lambda \times 621\lambda$
Digital resolution (S)	19 voxels mm^{-1}
Magnification (M)	0.38
Number of samples	14 000
Interrogation method	Sliding-average correlation
IV	$32 \times 16 \times 32$ voxels 1.68 mm × 0.84 mm × 1.68 mm $43\lambda \times 22\lambda \times 43\lambda$
IV overlap	75 %
Vectors per field	$38 \times 13 \times 57$

TABLE 3. System parameters of the time-resolved tomo-PIV.

The noise level of the current measurements is higher in comparison to the tomo-PIV velocity field of Ghaemi *et al.* (2012) which had a random noise level of 0.04 voxels (0.02 m s^{-1}). This higher random noise is mostly due to the larger measurement volume of the current tomo-PIV configuration (almost twice the thickness) which reduces the reconstruction quality due to the increase of the line of sight of each camera and consequently a higher number of ghost particles according to Elsinga (2008). In addition, the acceleration of fluid elements between the PIV exposures results in the main systematic error of PIV measurement, known as the truncation error. Boillot & Prasad (1996) modelled the truncation error and this was later adapted for symmetric window deformation by Ghaemi *et al.* (2012) and is estimated here to be about $\varepsilon_{u,sys} = 0.05$ voxels (0.03 m s^{-1}).

2.5. *PIV-based pressure evaluation*

The instantaneous pressure field is evaluated from the three-dimensional time-resolved velocity field by applying the Poisson pressure equation assuming incompressibility of the flow expressed as

$$\nabla^2 P = -\rho \boldsymbol{\nabla} \cdot \frac{\mathrm{D}\boldsymbol{U}}{\mathrm{D}t}, \tag{2.1}$$

where P represents the instantaneous pressure, $\boldsymbol{U}$ is the velocity vector and ρ is the fluid density. On the right-hand side the symbol $\mathrm{D}/\mathrm{D}t$ indicates the material derivative of the velocity field. Three-dimensional time-resolved measurement is required for accurate evaluation of this term in turbulent flow regimes. The Lagrangian method applied to calculate the material derivative has been proposed by Liu & Katz (2006) for planar measurements and is formulated as

$$\left.\frac{\mathrm{D}\boldsymbol{U}_p}{\mathrm{D}t}\right|_{(t_0)} \approx \frac{\boldsymbol{U}_{p(t_0+n\Delta t)} - \boldsymbol{U}_{p(t_0-n\Delta t)}}{2n\Delta t} \tag{2.2}$$

for a three-dimensional vector field. In this equation, $\boldsymbol{U}_p$ indicates the velocity of a fluid parcel travelling on a trajectory passing through a grid node at the location $\boldsymbol{X}_p$ at time t_0. The location of the fluid parcel at $t_0 + n\Delta t$ and $t_0 - n\Delta t$ is estimated by following the trajectory of the fluid parcel using the velocity vector $\boldsymbol{U}_p(t_0)$ forward and

backward in time, respectively. In the analysis of this work a time step of $3\Delta t$ ($n = 3$ and $\Delta t = 100$ μs) is considered based on the evaluation of Ghaemi *et al.* (2012).

The pressure evaluation from (2.1) is carried out using a Poisson solver applying a second-order central-difference scheme. The boundary conditions are enforced with a Neumann-type boundary at the wall and the four side boundaries (two XY-planes on the spanwise side and two YZ-planes on the streamwise side) from the incompressible momentum equation as

$$\nabla P = -\rho \frac{\mathrm{D}\boldsymbol{U}}{\mathrm{D}t}. \tag{2.3}$$

A Dirichlet-type boundary condition is applied at the XZ-plane of the free-stream side. At this boundary, a known pressure based on the average velocity field is estimated using the Bernoulli equation:

$$P_b = P_\infty + \tfrac{1}{2}\rho(U_\infty^2 - \langle U_b \rangle^2), \tag{2.4}$$

where P_∞ and U_∞ correspond to the free-stream condition while U_b and P_b are at the Dirichlet boundary location. This Dirichlet boundary condition is chosen within the turbulent boundary layer following the analysis of Ghaemi *et al.* (2012) which showed that there is a negligible effect on the calculated wall pressure if the Dirichlet boundary is lowered down to a wall-normal location of 0.2δ. Having obtained the right-hand side of (2.1) from the time-resolved tomo-PIV data, the volumetric integration follows

$$P_{(X,Y,Z)} = \iiint_{X,Y,Z} \nabla^2 P \,\mathrm{d}X\,\mathrm{d}Y\,\mathrm{d}Z = -\rho \iiint_{X,Y,Z} \left[\frac{\partial}{\partial X}\left(\frac{\mathrm{D}U}{\mathrm{D}t}\right) + \frac{\partial}{\partial Y}\left(\frac{\mathrm{D}V}{\mathrm{D}t}\right) + \frac{\partial}{\partial Z}\left(\frac{\mathrm{D}W}{\mathrm{D}t}\right) \right] \mathrm{d}X\,\mathrm{d}Y\,\mathrm{d}Z. \tag{2.5}$$

The integration results in three-dimensional pressure fields over a volume of (248^+, 113^+, 474^+) corresponding to tomo-PIV velocity measurements at a frequency of 10 000 Hz for a duration of 1.4 s.

The random error of the PIV-based pressure evaluation is estimated here following the method detailed by Ghaemi *et al.* (2012) based on the error of the velocity material derivative. The random error of the velocity field estimated in the last section introduces a random error of about $\varepsilon_{Lag,vel} = 85$ m s^{-2} in the estimation of the material derivative. The truncation error of the Lagrangian method is also considered here as a source of random error as it can cause overestimation or underestimation. Assuming the same velocity gradient within the turbulent field as Ghaemi *et al.* (2012) due to the similar Reynolds numbers, the truncation error of the Lagrangian method is estimated to be $\varepsilon_{Lag,trunc} = 78$ m s^{-2}. Therefore, the total error of the Lagrangian method is $\varepsilon_{Lag,rand} = \sqrt{\varepsilon_{Lag,vel}^2 + \varepsilon_{Lag,trunc}^2} = 115$ m s^{-2} which results in approximately 0.06 Pa uncertainty in the evaluation of the pressure fluctuations. This estimation is slightly lower than the random error of 0.12 Pa ($0.2p_{rms}$) observed in the PIV-based pressure power spectrum which is detailed in § 3. However, this noise level is well below the required accuracy of the current investigation since we are mainly interested in extreme pressure peaks where $|p|$ exceeds $2p_{rms}$ (∼1.2 Pa).

The PIV-based pressure is also evaluated in comparison to simultaneous wall-pressure measurements using the electret-condenser microphone as shown in figure 4. The comparison shows that tomo-PIV captures most of the features of the pressure

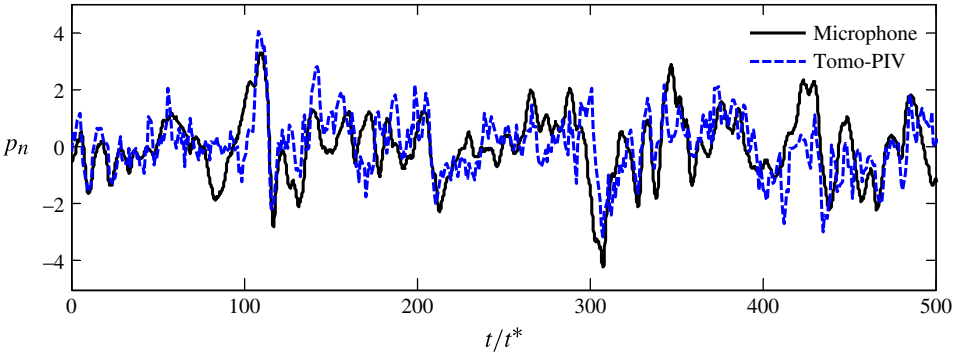

FIGURE 4. (Colour online) Simultaneous measurement of wall pressure (p_n) versus time using the microphone and the tomo-PIV system over $\Delta t/t^* = 500$ ($\Delta t = 0.5$ s).

signal and results in a reasonable agreement with the microphone signal. Further evaluation of the simultaneous pressure signals demonstrates that ∼70 % of the negative and positive HAPPs of the microphone wall pressure exists in the tomo-PIV-based pressure. The temporal cross-correlation coefficient between the two pressure signals is 0.51, slightly lower than that of Ghaemi *et al.* due to the larger tomo-PIV measurement volume.

2.6. *Conditional averaging*

The conditional-averaging technique introduced by Antonia (1981) is applied in the current investigation to characterize the turbulent structures associated with the HAPPs. The three-dimensional extension of this procedure has been recently applied to identify the buffer layer structures linked to the wall stress events by Sheng, Malkiel & Katz (2009). In the current investigation, local minima or maxima of wall pressure (p_w) are detected in the pressure fields obtained from the tomo-PIV. When the local extremum of wall pressure exceeds a certain threshold, the quantity C is sampled over a volume of $(290\lambda, 110\lambda, 140\lambda)$ centred at $(X_m, 55\lambda, Z_m)$ where X_m and Z_m are the wall coordinates of the local extremum. The positive wall-pressure peaks are conditionally averaged over the sampled volumes using

$$\hat{C} = \langle C \rangle | p_w(X_m, Z_m) > \alpha p_{rms}, \tag{2.6}$$

where $\langle\,\rangle$ denotes ensemble averaging, the hat sign denotes conditional averaging and α is a threshold limit. The coordinate system of the conditional averages is transferred to the centre of the samples in the XZ-plane and is indicated by x, y, z. Different C variables such as normalized fluctuating pressure $p_n = p/p_{rms}$ and velocity components U, V, W are considered. The negative wall-pressure samples are conditionally averaged using

$$\hat{C} = \langle C \rangle | p_w(X_m, Z_m) < -\alpha p_{rms}. \tag{2.7}$$

The threshold limit is $\alpha = 2$ in the current study for both the positive and negative HAPPs. This limit falls among the thresholds levels which were applied in the previous investigations. Schewe (1983) considered a threshold level of $\alpha = 3.2$. Johansson *et al.* (1987) investigated several thresholds ranging from 1 to 3.5 while conducting the bulk of the investigations using a threshold of $2.5p_{rms}$. Kim *et al.* (2002) applied a threshold level of $2p_{rms}$ to obtain conditional averages of the vorticity

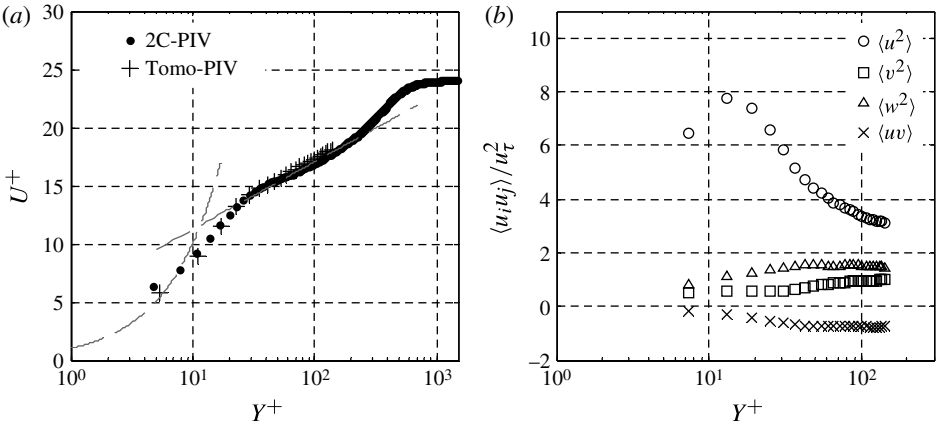

FIGURE 5. Semi-log profiles of (*a*) the mean streamwise velocity measured by both 2C-PIV and tomo-PIV systems and (*b*) the normal and shear Reynolds stress measured by tomo-PIV. The dashed lines show the law of the wall and the log law.

field. The selected threshold resulted in 3647 positive and 3887 negative samples obtained from different locations of the measurement volume. The analysis of the data shows that ∼40 % of the samples are related as they are advected structures through the time-resolved measurement. However, removing the related samples did not change the conditional averages as they are statistically converged.

The conditional averaging technique is also applied to the pressure field based on the detection of hairpin structures to investigate any possible bi-directional relation. The hairpin paradigm is one of the most prevalent organizations of structures within the turbulent boundary layer and includes several coherent structures such as ejections, sweeps, and the shear layer (Adrian 2007). In the current investigation, the hairpin structure is detected based on a strong ejection event characterized by $u < 0, v > 0$ at a threshold level of $uv/U_\infty^2 < -0.025$. The sampled hairpins are aligned relative to the centroid of the ejection event (local minima of uv) followed by the averaging procedure applied to both three-dimensional velocity and pressure fields.

3. Characterization of the turbulent boundary layer

The semi-logarithmic profiles of the turbulent boundary layer measured by the 2C-PIV and tomo-PIV systems demonstrate reasonable agreement between the two measurements as shown in figure 5(*a*). The 2C-PIV has a higher spatial resolution and larger wall-normal extent so as to obtain the inner layer variables of table 1. The measurement field of the tomo-PIV system resolves the sublayer, the buffer layer and part of the logarithmic layer. The normal and shear components of the Reynolds stress measured by the tomo-PIV system are shown in figure 5(*b*) demonstrating the expected trend of these fluctuations with a peak in the near-wall region. The peak of $\langle u^2 \rangle$ is around $Y^+ = 15$ which is in agreement with the measurements of Hussain & Reynolds (1975) at a similar Reynolds number.

The power spectral density (PSD) of the streamwise velocity fluctuations (E_{uu}) at different wall-normal distances is shown in figure 6(*a*). E_{uu} is normalized using the inner variable (u_τ^2) and multiplied by non-dimensional frequency (f^+) resulting in $f^+E_{uu}^+$ plotted versus f^+. The highest energy level, as expected, is observed around

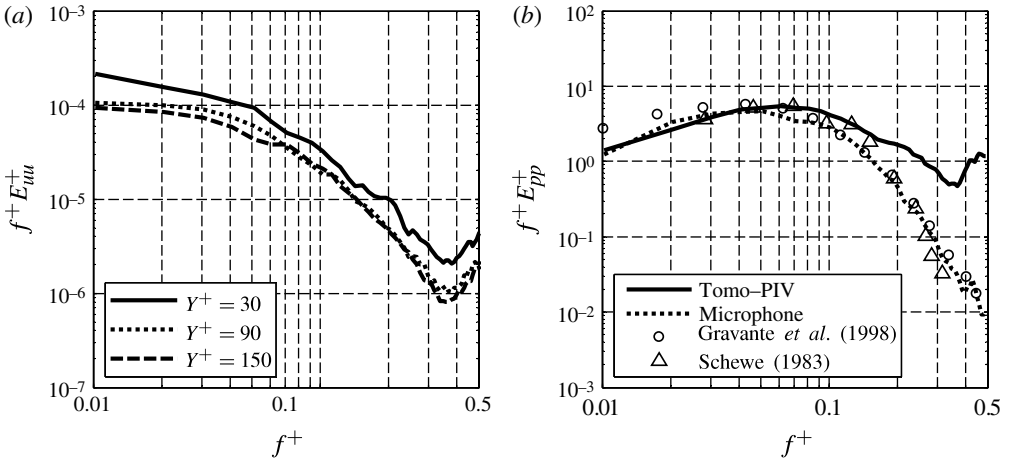

FIGURE 6. (*a*) Normalized pre-multiplied PSD of streamwise velocity fluctuation at different wall-normal locations. (*b*) Comparison of normalized pre-multiplied PSD of wall pressure from microphone measurement and tomo-PIV based pressure to that of previous investigations. The data of Schewe (1983) and Gravante *et al.* (1998) correspond to $Re_\theta = 1805$ and 1400, respectively.

the buffer layer region at $Y^+ = 30$ in comparison to the pre-multiplied PSDs at $Y^+ = 90$ and 150. The energy difference between the wall-normal locations is reduced at higher frequencies when considering the logarithmic and the pre-multiplied scale of the vertical axis. Also for each pre-multiplied PSD a reduction of the energy level is observed up to $f^+ = 0.35$ ($\sim$3500 Hz) where it reaches a minimum. This frequency shows the highest temporal resolution of the tomo-PIV measurement since beyond this limit, the random noise dominates and the pre-multiplied PSD increases. The noise level of the velocity fluctuations at $Y^+ = 30$ is approximately 0.05 m s^{-1} which is higher than the 0.03 m s^{-1} noise level at $Y^+ = 90$ and 150, possibly due to higher light scattering and velocity gradient near the wall surface.

The pre-multiplied PSDs of wall pressure measured by the microphone, the tomo-PIV-based pressure, and previous investigations are shown in figure 6(*b*). The pre-multiplied PSD of pressure fluctuations (f^+E_{pp}) is normalized using the inner variable ($\mu\rho^2 u_\tau^2$) resulting in $f^+E^+_{pp}$. The normalization using inner variables ensures the collapse of the pre-multiplied PSDs for different Reynolds numbers at high frequencies (Tsuji *et al.* 2007). However, the data of Gravante *et al.* (1998) and Schewe (1983) with comparable Re_θ is expected also to overlap at lower frequencies. The comparison shows good agreement with the microphone measurement at high frequencies while discrepancies are observed at lower frequencies. The difference could be due to background facility noise at low frequencies in different experiments or nonlinearity sensitivity of the current microphone for $f^+ < 0.25$.

The pre-multiplied PSD of the tomo-PIV shows a similar trend relative to the microphone signal up to $f^+ = 0.15$ ($\sim$1500 Hz) where the tomo-PIV pressure deviates from the microphone measurement. At this frequency ($f^+ = 0.15$), the error relative to the microphone measurement is $\sim$50 %. The deviation occurs earlier than that of the pressure evaluation in figure 9(*a*) of Ghaemi *et al.* (2012), where it occurs at about $f^+ = 0.35$ ($\sim$3500 Hz). As explained before, the higher noise level of the current experiment is due to its larger measurement volume (almost twice in the

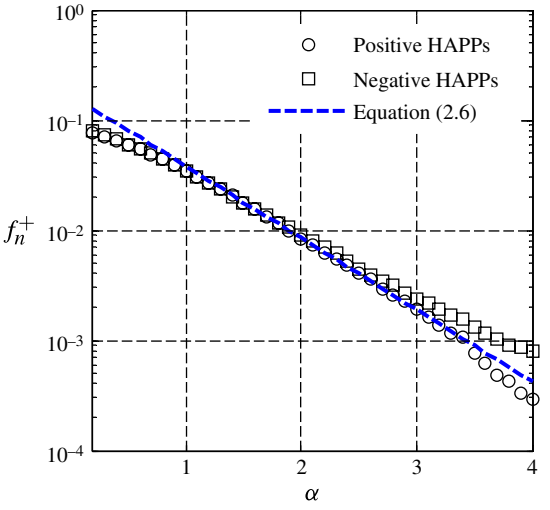

FIGURE 7. (Colour online) The occurrence frequency of the positive and negative HAPPs versus the HAPP detection threshold (α).

tomo-PIV depth direction). The noise level becomes dominant similarly to the velocity pre-multiplied PSD at $f^+ = 0.35$ (~3500 Hz) where it reaches a minimum indicating a random noise level of 0.12 Pa.

The energy of the HAPPs is expected to spread over a broad frequency range due to the impulsive shape of the HAPPs as was shown in figure 1. Nevertheless, a characteristic time (T_{ch}) and frequency (f_{ch}) is of interest to investigate their relation to other coherent structures and for flow control purposes. Both Schewe (1983) and Johansson *et al.* (1987) estimated the characteristic frequency based on the reciprocal of peak duration. Although they applied high peak detection thresholds ($>2.5p_{rms}$), scrutinizing their plots (figure 16 of Schewe 1983 and figure 3 of Johansson *et al.* 1987) shows that they estimated the peak duration with a much lower threshold level that is not indicated. Using this lower threshold, Johansson *et al.* (1987) suggested a characteristic frequency in the range of $f_{ch}^+ = 0.07$–0.1 which agrees with $f_{ch}^+ = 0.08$ estimated by Schewe (1983). Conditional averaging of the high-amplitude peaks and estimation of their duration in the current experiment, with a threshold of $2p_{rms}$, results in a characteristic time of $T_{ch}^+ = 2.6$ for the positive and negative HAPPs. This corresponds to a characteristic frequency of $f_{ch}^+ = 0.39$ which is higher than the estimations of Schewe (1983) and Johansson *et al.* (1987) due to the threshold level. However, if the conditional averaging of the high-amplitude peaks is conducted based on the threshold of $2p_{rms}$ and an estimation of their duration using a lower threshold of $0.5p_{rms}$ closer agreement is observed. The result shows characteristic times of $T_{ch}^+ = 9.9$ ($f_{ch}^+ = 0.10$) and 9.3 ($f_{ch}^+ = 0.11$) for the positive and negative HAPPs, respectively.

Johansson *et al.* (1987) conducted a sensitivity analysis on the occurrence frequency (f_n^+) of the HAPPs as a function of the threshold level and observed exponential behaviour of f_n^+. Their analysis showed similar occurrence frequencies for both positive and negative HAPPs while f_n^+ varied from 0.0002 up to 0.02 for thresholds reducing from $4p_{rms}$ to $1p_{rms}$. The semi-log plot of f_n^+ versus the threshold level shown in figure 7 agrees with the results of Johansson *et al.* (1987). The occurrence

	Re_θ	p_{rms}/q	s	k
Tomo-PIV	1900	0.012	−0.03	3.88
Microphone	1900	0.010	−0.12	4.54
Gravante *et al.* (1998)	1580	0.010	−0.06	4.20
Gravante *et al.* (1998)	1810	0.009	−0.04	4.15
Schewe (1983)	1400	0.010	−0.18	4.80

TABLE 4. Comparison of the statistics of wall-pressure fluctuations obtained from the surface microphone and tomo-PIV with previous investigations.

frequency can be estimated using an exponential fit through

$$f^+ = A\mathrm{e}^{B\alpha} \tag{3.1}$$

for both the positive and negative HAPPs where $A = 0.17$ and $B = -1.5$ for the threshold level between $\alpha = 1$ and about $\alpha = 2.5$. Beyond $\alpha = 2.5$ the occurrence frequency of the negative HAPPs is higher than the positive ones. This difference has not been observed in the analysis of Johansson *et al.* (1987) perhaps due to attenuation of the high-amplitude peaks at the surface of their relatively large microphone (64λ). The higher number of negative HAPPs has been noticed by Schewe (1983) by analysing the skewness factor of wall pressure for different sensor sizes. Schewe (1983) observed that the higher occurrence of negative HAPPs is only visible for sensors smaller than 39λ. Similar to figure 7, Schewe (1983) observed that the occurrence frequency of the negative HAPPs is larger than that of the positive HAPPs when the threshold is increased beyond $\alpha = 2$. An occurrence frequency of approximately $f_n^+ = 0.01$ is estimated for both the positive and negative HAPPs at $\alpha = 2$. Although this frequency is in the high-energy part of the pre-multiplied PSD of figure 6, the HAPPs energy is expected to be spread over a large frequency range considering that the HAPPs contribute 60 % of the p_{rms} energy.

Further statistical evaluation of the current experiment relative to the previous investigations is demonstrated in table 4 using p_{rms} normalized by dynamic pressure ($q = 0.5\rho U_\infty^2$), skewness (s), and kurtosis (k). The p_{rms}/q value of the PIV-based pressure is slightly higher than that of the current microphone measurement and the previous investigations. The higher p_{rms} is associated with the noise of the PIV measurement starting from $f^+ = 0.15$ as was observed in the PSD of figure 6(*b*). The skewness factor is a measure of asymmetry in data distribution. There is a considerable discrepancy in the skewness quantities shown in table 4, the negative value of the tomo-PIV pressure and the other measurements indicate that there is a higher number of negative wall-pressure fluctuations in the turbulent boundary layer. The kurtosis or flatness factor of the tomo-PIV pressure is observed to be slightly lower than the other measurements indicating a lower number of peaks in the extreme positive and negative tails of the pressure distribution. Visual observation of the data also shows that the tomo-PIV pressure signal rarely exceeds $3p_{rms}$ while the microphone pressure signals show that the HAPPs occasionally exceed $5p_{rms}$. The occurrence of HAPPs up to $7p_{rms}$ has been reported by Schewe (1983) and Haritonidis *et al.* (1988). The slight damping of extreme HAPPs by tomo-PIV is attributed to the spatio-temporal filtering effects of the PIV technique and also the Lagrangian calculation of the material derivative.

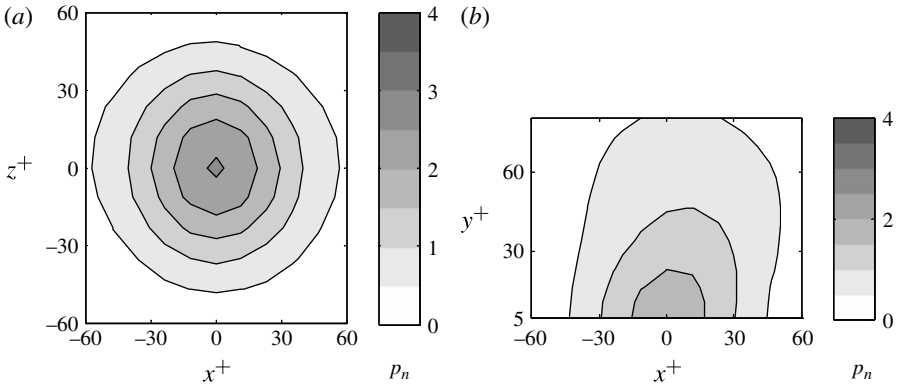

FIGURE 8. Conditional average of positive HAPPs in (*a*) *xz*- and (*b*) *xy*-planes.

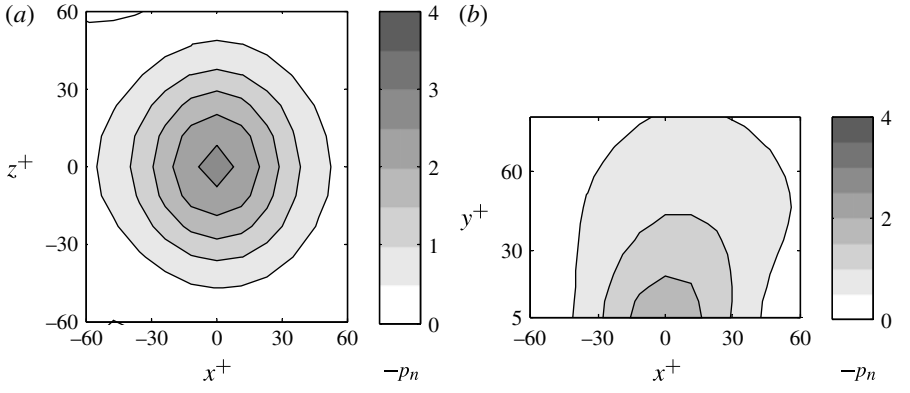

FIGURE 9. Conditional average of negative HAPPs in (*a*) *xz*- and (*b*) *xy*-planes.

4. Spatio-temporal scales of HAPPs

The spatio-temporal scales of the HAPPs are studied in this section using the conditionally sampled three-dimensional velocity and pressure fields detailed in § 2.6. The previous experimental investigations have only evaluated the wall region using a dense array of microphones. As a result, three-dimensional evaluation of the HAPPs has been limited to numerical simulations. The conditionally averaged normalized pressure for positive and negative HAPPs is illustrated in figures 8 and 9, respectively. The peak of the average pressure reaches $3p_{rms}$ for both positive and negative HAPPs in the *xz*-plane of figures 8(*a*) and 9(*a*), which shows that the pressure events are well beyond the threshold level ($\alpha = 2$). The peak of the negative HAPPs ($p_n < -4$) in the *xz*-plane appears to be slightly larger than the positive HAPPs, which is associated with the uncertainty of pressure evaluation.

In the *xy*-plane, an inclination of approximately 70° with respect to the streamwise direction is observed which is higher than the inclination of typical vortical structures within the boundary layer. For example the hairpin vortices are inclined at ∼45° (Head & Bandyopadhyay 1981) and shear layers are reported to have angles less than 45° inclination relative to the free stream (Liu *et al.* 1991; Adrian, Meinhart & Tomkins 2000). The higher inclination angle of the average pressure field is associated with the

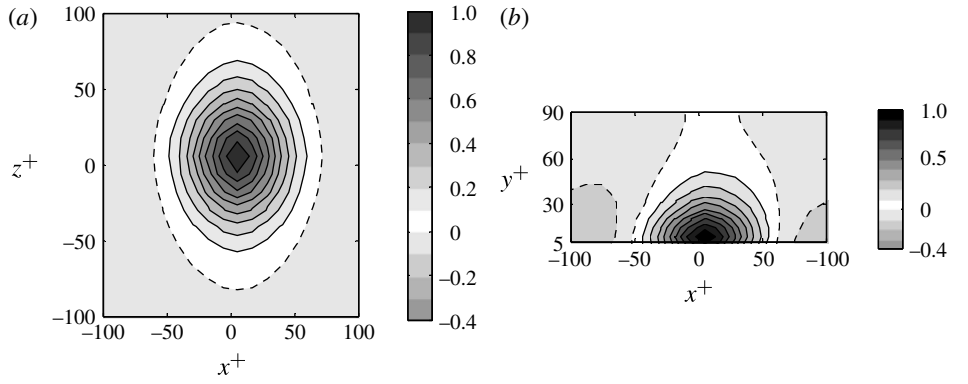

FIGURE 10. Contours of constant space-correlation of wall pressure: (*a*) $R_{pp(\Delta x,0,\Delta z}$ in the *xz*-plane and (*b*) $R_{pp(\Delta x,\Delta y,0)}$ in the *xy*-plane for the unconditioned data. The conditional averages of positive and negative HAPPs showed similar results. The dashed boundaries specify negative contours.

non-local characteristic of the pressure field. A strong pressure fluctuation is evenly spread in all radial directions which results in a higher inclination angle of the average pressure contour with respect to the corresponding turbulent structure. Nevertheless, the sloped average pressure in the *xy* contours indicates the correspondence of both the positive and negative HAPPs to the inclined structures of a turbulent boundary layer.

The three-dimensional spatial scale of the HAPPs is further studied by applying the spatial correlation function to the conditionally selected volumes using the relation

$$R_{CC(\Delta x,\Delta y,\Delta z)} = \frac{\langle C_{(x,y,z}C_{(x+\Delta x,y+\Delta y,z+\Delta z)}\rangle}{\sqrt{\langle C^2_{(x,y,z}\rangle\langle C^2_{(x+\Delta x,y+\Delta y,z+\Delta z)}\rangle}}. \tag{4.1}$$

The variable C is chosen to be the pressure and the velocity fluctuations. The contours of R_{pp} of the unconditioned ensemble in the *xz*- and *xy*-planes are shown in figures 10(*a*) and 10(*b*), respectively. The corresponding contours of the conditioned averages of the positive and negative HAPPs were similar and are not presented here for brevity. The spatial correlation shows a radially symmetric field in the vicinity of the centre for radii less than 30λ in the *xz*-plane, which is due to the spatial resolution and overlap of tomo-PIV interrogation volumes. With increase of the radius and reduction of R_{pp} the spanwise scale exceeds the streamwise scale and blobs are extended 130λ and 180λ in the *x*- and *z*-directions (measured at $R_{pp} = 0$), respectively. Similar anisotropic behaviour for small R_{pp} isocontours has also been observed by the transducer array of Bull (1967) and also the DNS study of Na & Moin (1998). The analysis of Kim (1989) based on DNS of a channel reports an isotropic distribution of R_{pp} at the wall and also at $y^+ = 50$ while significant spanwise elongation of the isocontours appears at a higher wall-normal distance of $y^+ = 180$. The wall-normal extent of the structures for the unconditioned case, positive HAPPs and the negative HAPPs is estimated between 70λ–90λ.

The occurrence of packets of HAPPs containing fluctuations of opposite signs is also evident from the negative R_{pp} regions. The negative R_{pp} is stronger in the streamwise direction of the conditioned HAPPs suggesting a stronger arrangement of positive and negative blobs in the streamwise direction. This alternating behaviour is consistent with the visual observation of Schewe (1983) and Ghaemi *et al.* (2012)

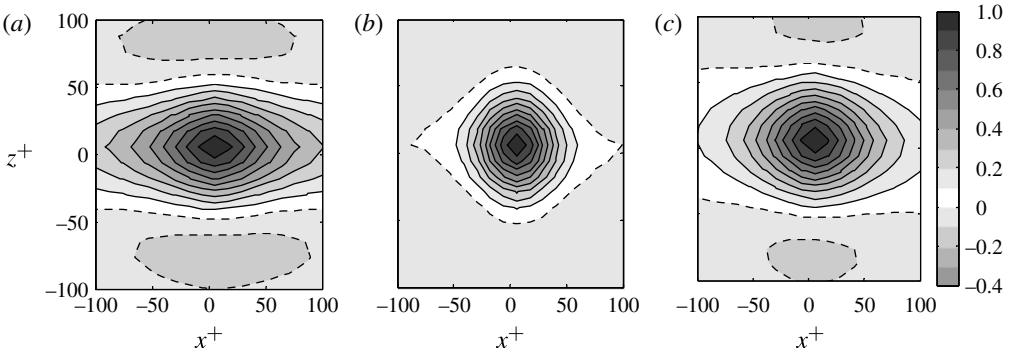

FIGURE 11. Contours of constant space-correlation of (*a*) R_{uu}, (*b*) R_{vv} and (*c*) R_{ww} in the *xz*-plane of the *u* velocity fluctuations for the unconditioned ensemble. The conditional average of positive and negative HAPPs show identical contours. The dashed boundaries specify negative contours.

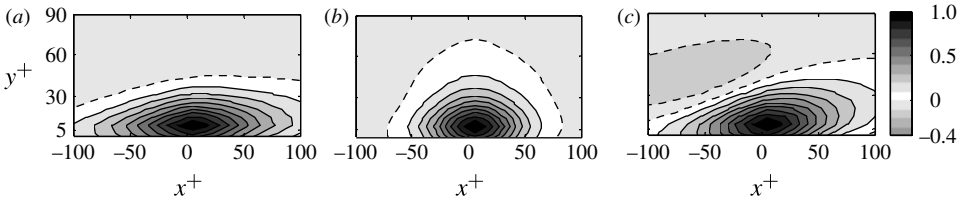

FIGURE 12. Contours of constant space-correlation of (*a*) R_{uu}, (*b*) R_{vv} and (*c*) R_{ww} in the *xy*-plane of the *u* velocity fluctuations for the unconditioned ensemble. The conditional average of positive and negative HAPPs show similar contours. The dashed boundaries specify negative contours.

who observed that two or more HAPPs of alternating signs may occur in succession. However, as the level of negative correlation suggests, the occurrence probability of the packets of HAPPs with alternating signs is low. Johansson *et al.* (1987) reported that only 7 % of the detected HAPPs occur in pairs for which both peaks exceed their threshold level of $2.33p_{rms}$. Similar to the average pressure fields of the HAPPs, the pressure structures are observed to be linked to the sloped structures of the turbulent boundary layer due to the inclined R_{pp} contours in the *xy*-planes of figure 10(*b*).

In order to compare the spatial scales of the HAPPs with the flow structure, R_{CC} isocontours of velocity fluctuations *u*, *v*, and *w* are demonstrated in the *xz*- and *xy*-planes of figures 11 and 12, respectively. The isocontours belong to the unconditioned ensemble; however, they are similar to the R_{CC} isocontours of the conditional average of positive and negative HAPPs. The resemblance of R_{CC} contours of the unconditioned ensemble and the conditionally sampled data of positive and negative HAPPs suggests that there is no correspondence between the HAPPs and a specific arrangement of the low- and high-speed streaks within the turbulent boundary layer. The most important feature revealed by the R_{uu} isocontours of figure 11(*a*) is the streak spacing, defined as twice the distance between adjacent low- and high-speed streaks. This streak spacing estimated as twice the distance between $R_{uu} = 1$ and the centroid of the negative R_{uu} region in figure 11(*a*) is $\sim 160^+$ comparable to the

streak spacing of 145^+ reported by Smith & Metzler (1983) at $y^+ = 30$ and the 150^+ estimated by Kim (1989). The streak spacing is invariant with respect to Reynolds number and is estimated to be $\sim 100^+$ for the streaks in the sublayer while it increases with wall-normal distance (Smith & Metzler 1983).

An isotropic distribution of R_{vv} is observed in figure 11(*b*) and also in the *xy*-plane of figure 12(*b*). The wall-normal velocity fluctuations occur as part of the ejection or sweep events which are stronger when a focused induction takes place. A focused ejection event occurs between the two quasi-streamwise sections (legs) of a hairpin vortex or between two counter-rotating streamwise vortices which typically interact in the inner layer (Robinson 1991). The result of these wall-normal fluctuations is observed as an isotropic distribution of R_{vv} for all the three ensembles. On the other hand, the isocontours of R_{ww} are elongated in the streamwise direction since the major contribution to spanwise velocity fluctuations is due to streamwise vortices. Although the negative correlation and the symmetric pattern of R_{ww} in figure 11(*c*) suggest the existence of counter-rotating vortices within the inner layer, these vortices are not always in pairs (Kim, Moin & Moser 1987; Sheng *et al.* 2009). The negative blob of R_{ww} at $x^+ = -30$ confirms the dominant contribution of vortices to the spanwise velocity fluctuations. It is also observed in figure 12(*c*) that the vortices are inclined.

The space–time correlation of the wall pressure has been applied since the early studies to estimate the mean advection velocity and consequently the wall-normal location of the pressure sources. The method has been insightful although the assumptions of a single pressure source and projection on the mean velocity profile should be carefully considered. In this study, we do not follow this method to characterize the source structures since three-dimensional measurement of the pressure and the velocity field is available. However, estimation of the mean advection velocity of the HAPPs is beneficial in arranging the sensors and actuators for future control systems. In order to conduct the analysis a planar realization of the pressure field $p_{(x,t)}$ with dimensions of $80\lambda \times 50\lambda$ $(x \times y)$ holding the HAPP at $x^+ = 40$ and $y^+ = 0$ is considered and the space–time correlation is conducted using

$$R_{pt(\Delta x,\Delta t)} = \frac{\langle p_{(x,t)} p_{(x+\Delta x,t+\Delta t)} \rangle}{\sqrt{\langle p^2_{(x,t)} \rangle \langle p^2_{(x+\Delta x,t+\Delta t)} \rangle}}. \tag{4.2}$$

The obtained R_{pt} isocontours of the positive and negative HAPPs and the unconditioned ensemble are shown in figures 13(*a*), 13(*b*) and 13(*c*),respectively.

The R_{pt} unconditioned ensemble isocontours of figure 13(*a*) show an increase of advection velocity with increase of streamwise distance from $\sim 12u_\tau (0.51U_\infty)$ at $R_{pt} = 0.6$ up to $16u_\tau (0.68U_\infty)$ at $R_{pt} = 0.2$. This trend which is proportional to the inverse of the slope of the thick dashed lines in figure 13 is associated with the gradual decay of small-scale high-frequency structures which travel slower in the vicinity of the wall (Townsend 1976; Perry, Henbest & Chong 1986). The remains are the structures with a longer lifetime (lower frequency) that travel at a higher velocity at locations further away from the wall. The increase in the advection velocity with streamwise separation has also been observed by Willmarth & Wooldridge (1962) and Bull (1967) using arrays of pressure transducers. For two transducers of small streamwise separation ($\sim\theta$), Willmarth & Wooldridge (1962) observed an advection velocity of $0.56U_\infty$ and Bull (1967) observed $0.53U_\infty$ while both estimated $0.83U_\infty$ for transducers of larger streamwise separation ($\sim 8\theta$, beyond the measurement field of the current experiment) and attributed the trend to the decay of the high-frequency pressure fluctuations.

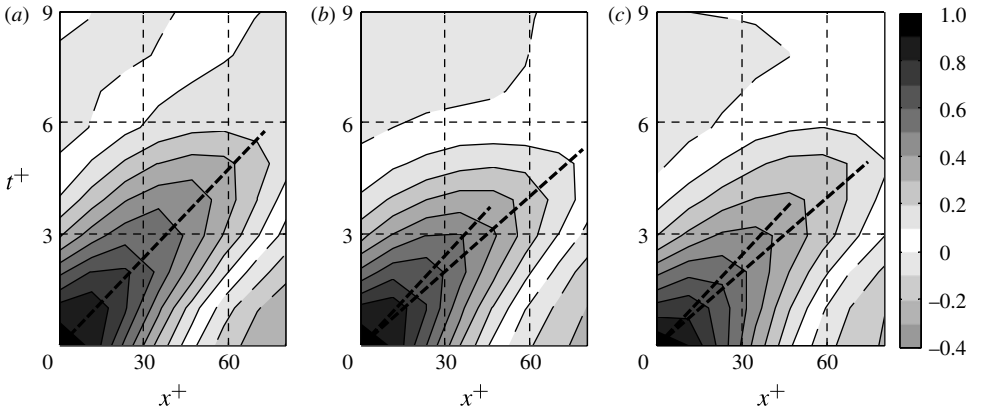

FIGURE 13. Isocontours of streamwise space–time correlation (R_{pt}) for (a) the unconditioned realizations, (b) the positive and (c) the negative HAPPs. The dashed lines show the approximate linear trajectory of least decay of R_{pt}. The dashed boundaries of the contours specify negative values.

Both the positive and negative HAPPs in figure 13(*b,c*) demonstrate relatively constant advection velocity along the streamwise direction. Therefore, the HAPPs and their corresponding turbulent structures possess a high temporal coherence (lifetime). Their advection velocity is $\sim 14.3u_\tau$ ($0.6U_\infty$) within the investigated streamwise distance of 80λ (1θ). Scrutiny of the space–time correlation plot of Schewe (1983) (figure 16 of that reference) shows an advection velocity of $14u_\tau$ within the first 75λ of streamwise distance which is in agreement with the current investigation. However, Schewe (1983) estimated a lower advection velocity of $11.9u_\tau$ ($0.53U_\infty$) over a streamwise distance of 225λ for both positive and negative HAPPs through phase averaging of high-amplitude events. The unexpected reduction of advection velocity could be due to broadening of the peak of the phase-averaged events at higher streamwise distances.

5. Instantaneous organization of the HAPPs

In this section, the instantaneous samples of the flow structures generating the negative and positive HAPPs are investigated. The samples are selected from visual examination of the tomo-PIV realizations revealing the most frequent structures. This type of analysis can be a subjective process and should be accompanied by statistical analysis similar to that described in the next section. This approach prevents erroneous conclusions due to the subjective bias involved in instantaneous viewing of the data or the misleading artifacts of averaging in conditional analysis.

5.1. *Unsteady organization*

A sample of the unsteady organization of the coherent structures of the velocity field and also the HAPPs obtained from tomo-PIV measurements is shown in figure 14. The low- and high-speed streaks are observed as elongated alternating streaks with spacing between 100λ–200λ. The high-speed streaks are occasionally wider than the low-speed streaks (within the inner layer) as observed on right-hand side ($Z^+ > 0$) of figure 14(*a*) and also based on our visual inspection of the data. Strong quasi-streamwise and a few spanwise vortical structures are observed in the visualization of the vortical

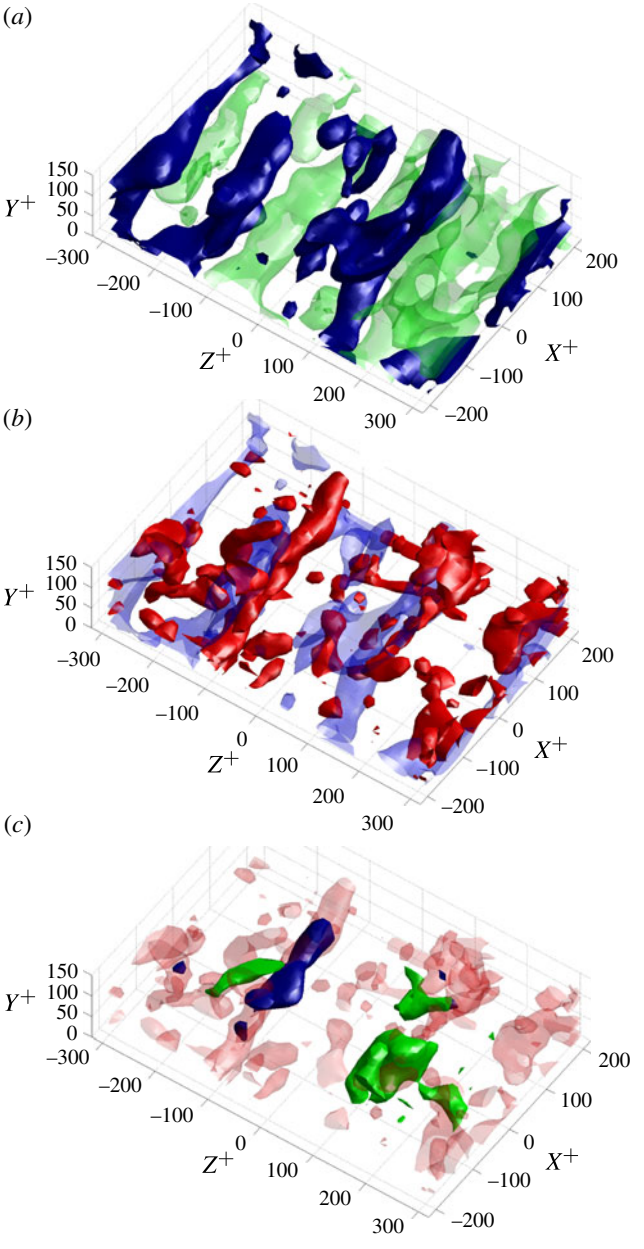

FIGURE 14. (Colour online) Unsteady organization of the coherent structures and the high-amplitude pressure peaks within the turbulent boundary layer measurement by tomo-PIV at $Re_\theta = 1900$. (*a*) The low- and the high-speed streaks are visualized by blue (dark grey) and green (light green) isosurfaces at $u/U_\infty = \pm 0.08$, respectively. (*b*) The low-speed streaks visualized as transparent blue (light grey) and the vortical structures identified at $Q = 0.3 \times 10^6\ \mathrm{s}^{-2}$ by red (dark grey) isosurfaces. (*c*) The vortical structures are shown in transparent red (light grey), the negative HAPPs in blue (dark grey) isosurfaces at $-3p_{rms}$ and positive HAPPs at $+3p_{rms}$ in green (medium grey) isosurfaces. The pressure field is only available from $X^+ = -120$ to $+120$.

structures in figure 14(*b*) using the *Q*-criterion (Hunt, Wray & Moin 1988). The quasi-streamwise vortices are linked to the low-speed streaks as they partially surround them. The ejection of the fluid away from the wall by these vortices lifts up the low-speed streaks to upper layers. On the other hand, no apparent connection between the spanwise vortices and the available low- or high-speed streaks is observed. The spanwise vortices are in the immediate vicinity of the wall which is in agreement with the observations of Sheng *et al.* (2009) of the inner layer structures ($Y^+ < 100$). The spanwise-oriented vortices are typically associated with the head of the hairpin vortices and consequently interact with the low-speed streaks. They may also correspond to the early stages of the development of a hairpin vortex or a pair of counter-rotating quasi-streamwise vortices (Sheng *et al.* 2009). Therefore, the lift-up (burst) of the low-speed flow from the viscous sublayer has not occurred yet or the thin streak is not detectable due to the limited spatial resolution of the measurement. The HAPPs shown in figure 14(*c*) suggest the low wavenumber (or frequency) of occurrence of these events in agreement with the previous studies (Johansson *et al.* 1987). However, both positive and negative HAPPs are spatially coherent. The observed negative HAPP shows strong overlap with the quasi-streamwise vortex while no apparent connection is observed between the positive peak and the vortical structures.

5.2. *Positive peaks*

The inspection of the instantaneous realizations suggests that the positive HAPPs are typically surrounded by vortical structures, especially in the downstream locations. An instantaneous sample of a positive HAPP and the surrounding vortical structures is shown in figure 15(*a*) using the *Q*-criterion. The observed vortical structures consist of a hairpin vortex downstream and a partially spanwise vortex upstream of the positive HAPP. This vortical organization is accompanied with an upstream sweep of high-speed fluid encountering the downstream ejection of low-speed fluid induced by the hairpin vortex. The formation of a focused ejection event by induction through the hairpin category of vortices has been extensively investigated in the literature (Adrian 2007). The interaction of the ejection event with the opposing flow forms a thin shear layer characterized by changes in $\partial u/\partial x$, $\partial u/\partial y$ as observed in figure 15(*b*). The shear layer is also observed to be strongly asymmetric in the spanwise direction. Johansson *et al.* (1987) noticed this spanwise asymmetry and emphasized its dynamical significance in the generation of strong shear layers in the y-direction.

The centre of the positive HAPP is at the lower side of the shear layer at about $y^+ = 10$ where a stagnation point is observed. This high-pressure stagnation point causes deceleration ($\mathrm{D}U/\mathrm{D}t < 0$ and $\mathrm{D}V/\mathrm{D}t < 0$) of the high-speed flow at the upstream region of the shear layer as observed in the Lagrangian acceleration vector field ($\mathrm{D}U/\mathrm{D}t, \mathrm{D}V/\mathrm{D}t$) of figure 15(*c*). The acceleration field is obtained here using (2.2) based on the three-dimensional Lagrangian method. The strong positive acceleration ($\mathrm{D}U/\mathrm{D}t > 0$) in the immediate downstream region of the shear layer (about $x^+ = 30$) shows deceleration of the ejection motion towards the upstream direction in the fluctuating velocity field. A significant spanwise deceleration of the fluid in the positive z-direction from $z^+ = -60$ to 0 is also observed in figure 15(*e*) which indicates asymmetric dynamics of the shear layer. Choi (1989) observed that inhibition of this asymmetry is the key mechanism in reduction of turbulence production and consequently skin friction over riblet surfaces. The yz-plane of figure 15(*f,g*) shows the positive HAPP between the two streamwise vortex components.

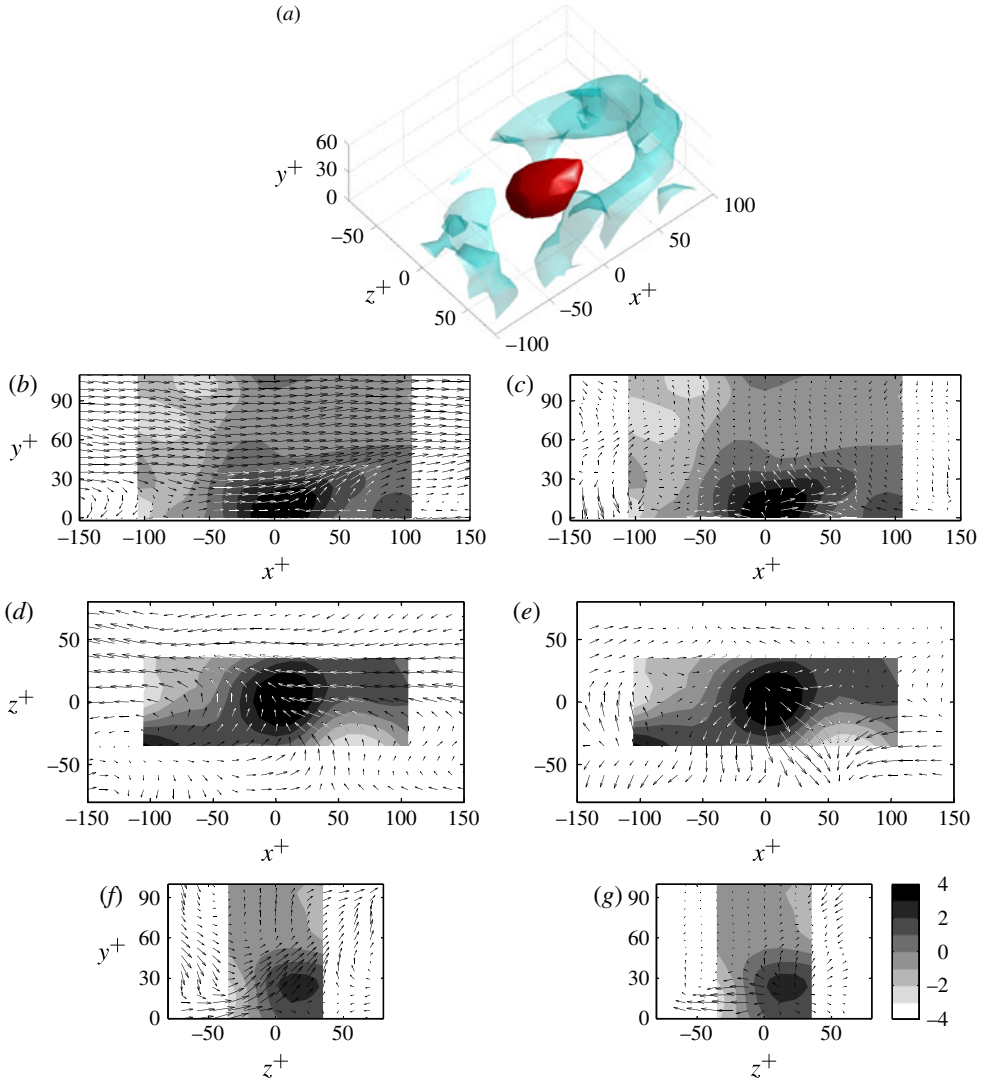

FIGURE 15. (Colour online) (*a*) An instantaneous visualization of a positive HAPP at $p_n = 3$ and the surrounding vortical structures including a hairpin vortex downstream of the HAPP identified by $Q = 0.5 \times 10^6$ s^{-2}. (*b,d,f*) The velocity vector fields with background isocontours of pressure over planes (*b*) *xy*, (*d*) *xz*, and (*f*) *yz*. (*c,e,g*) The material derivative (DU/Dt, DV/Dt, DW/Dt) vector obtained using the Lagrangian method with background isocontours of pressure over planes (*c*) *xy*, (*e*) *xz*, and (*g*) *yz*. The *xz*-plane crosses at $y^+ = 20$ and the *yz*-plane crosses at $x^+ = 50$.

The visual inspection of positive HAPPs reveals a significant connection with the hairpin vortices through the formation of the shear layers and the consequent stagnation point. Although the complete hairpin vortex shown in figure 15 is not a frequent occurrence, derivatives such as a spanwise vortex along with a quasi-streamwise segment on a side is typically observed in the instantaneous visualizations. Figure 16 shows a sample of such a vortex inducing an ejection event which opposes the upstream inrush of high-speed flow. The shear layer shows strong $\partial u/\partial x$, $\partial u/\partial y$

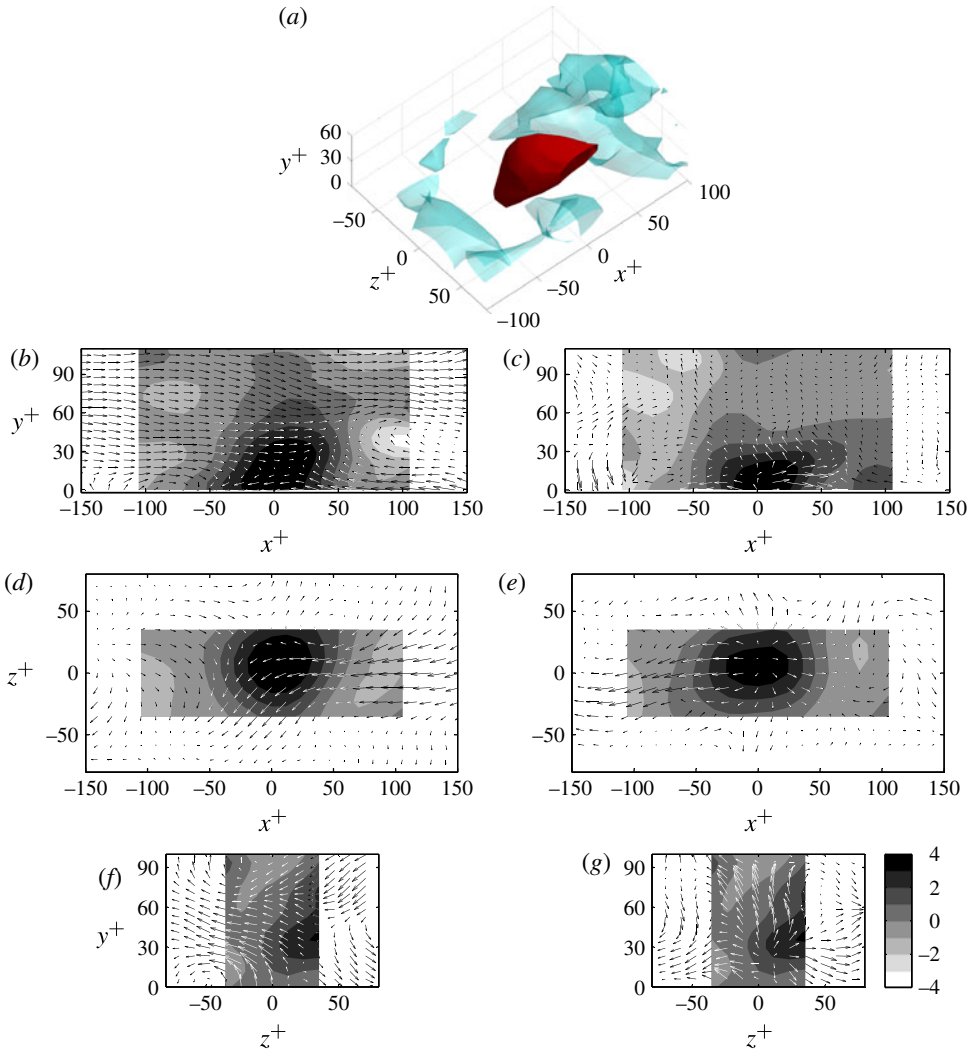

FIGURE 16. (Colour online) (*a*) An instantaneous visualization of a positive HAPP at $p_n = 3$ and the surrounding vortical structures identified by $Q = 0.5 \times 10^6\ \mathrm{s}^{-2}$. The velocity vector fields with background isocontour of pressure over planes (*b*) *xy*, (*d*) *xz*, and (*f*) *yz*. The material derivative $(\mathrm{D}U/\mathrm{D}t, \mathrm{D}V/\mathrm{D}t, \mathrm{D}W/\mathrm{D}t)$ vector obtained using the Lagrangian method with background isocontours of pressure over planes (*c*) *xy*, (*e*) *xz*, and (*g*) *yz*. The *xz*-plane crosses at $y^+ = 20$ and the *yz*-plane crosses at $x^+ = 0$.

and $\partial u/\partial z$ and a stagnation point overlapping with the peak of the high-pressure region. The acceleration fields in figure 16(*c*,*e*) demonstrate strong deceleration acting on both the sweep and the ejection events in the negative and positive *x*-directions, respectively. Unlike figure 15, there is a strong symmetry with respect to the $x^+ = 0$ line in figure 16(*c*,*e*). This behaviour suggests that vortices with dominant spanwise vorticity form relatively symmetric shear layers while the presence of quasi-streamwise vortices, in inducing the focused ejection, promotes asymmetric behaviour.

5.3. *Negative peaks*

The visual inspection of three-dimensional samples suggests a strong connection between the negative HAPPs and vortical structures. An instantaneous sample of a quasi-streamwise vortex with a strong negative HAPP ($p_n = -3$) at its core is illustrated in figure 17(*a*). This quasi-streamwise vortex is slightly tilted in the spanwise direction and is inclined at approximately 30° with respect to the x-axis. The vortex is initiated in the vicinity of the wall and extends up to the upper wall-normal limit of the measurement volume. The intense part of the negative HAPP at about $y^+ = 20$ overlaps with the lower portion of the vortex.

Two positive pressure fluctuations are observed at both upstream and downstream locations of the negative HAPP in figure 17(*b*). The velocity field of this figure shows a large-scale sweep event initiated from the logarithmic region and extended approximately from $x^+ = -100$ to 100 in the streamwise direction. This large-scale sweep event may be related to the strong negative HAPP which accelerates the flow from the upper layers towards the wall and is perhaps the same type of sweep event as observed by Johansson *et al.* (1987). However, it does not appear to be the source of the negative HAPP since the sweep region also covers the two positive-pressure blobs. The limitation of Johansson *et al.* (1987)'s analysis to two velocity components at a single streamwise location may have concealed the vortical structures. A vortex is defined as a coherent region in space with excess of vorticity in comparison to the shear strain rate (Jeong & Hussain 1995) and it is difficult to detect this spatial feature by point-wise measurement of velocity. However, the velocity field in the xz-plane of figure 17(*d*) confirms the coincidence of the negative HAPP with the centroid of the wall-normal swirling motion as the outward radial acceleration from the vortex centroid should be balanced by the pressure gradient.

The acceleration vector $(\mathrm{D}U/\mathrm{D}t, \mathrm{D}W/\mathrm{D}t)$ in the xy-plane of figure 17(*c*) shows strong acceleration of the flow in both positive x- and negative y-directions towards $(x^+, y^+) = (15, 25)$ which is the centroid of the negative HAPP and the vortex core. Acceleration towards the centroid of the vortex consisting of a strong spanwise component is also observed in the xz-plane of figure 17(*e*). Downstream of the negative pressure peak, the acceleration region is followed by a recovery region in which pressure increases. The yz-plane of figure 17(*f*) demonstrates the streamwise component of the quasi-streamwise vortex and the high-acceleration region of figure 17(*g*) both coinciding with the low-pressure region.

The association of the negative HAPPs with vortical structures is not limited to the quasi-streamwise vortices. The visual inspection demonstrates negative HAPPs also overlapping with the spanwise vortical structures. A sample of a negative HAPP formed within the swirling centre of a spanwise vortex is shown in figure 18. The peak of the HAPP is adjacent to the wall and approximately at $y^+ = 5$. No large-scale sweep event is observed in figure 18(*b*) which contradicts the conclusion of Johansson *et al.* (1987). The structure is observed to be coherent in the spanwise direction as shown in figure 18(*d*). The negative HAPP is surrounded by two strong positive HAPPs at upstream and downstream streamwise locations showing a successive arrangement of HAPPs which is also observed by Schewe (1983) and Johansson *et al.* (1987). The three successive HAPPs may communicate with each other since the acceleration region of the negative HAPP is also the recovery region of the upstream positive HAPP as observed at $x^+ = -25$ of figure 17(*c,e*).

The streamwise alternating arrangement of the positive and negative HAPPs observed in figure 18(*b*) requires further attention. There is a positive HAPP at $x^+ = -55$, a negative HAPP at $x^+ = 0$, a positive HAPPs at $x^+ = 55$ and there

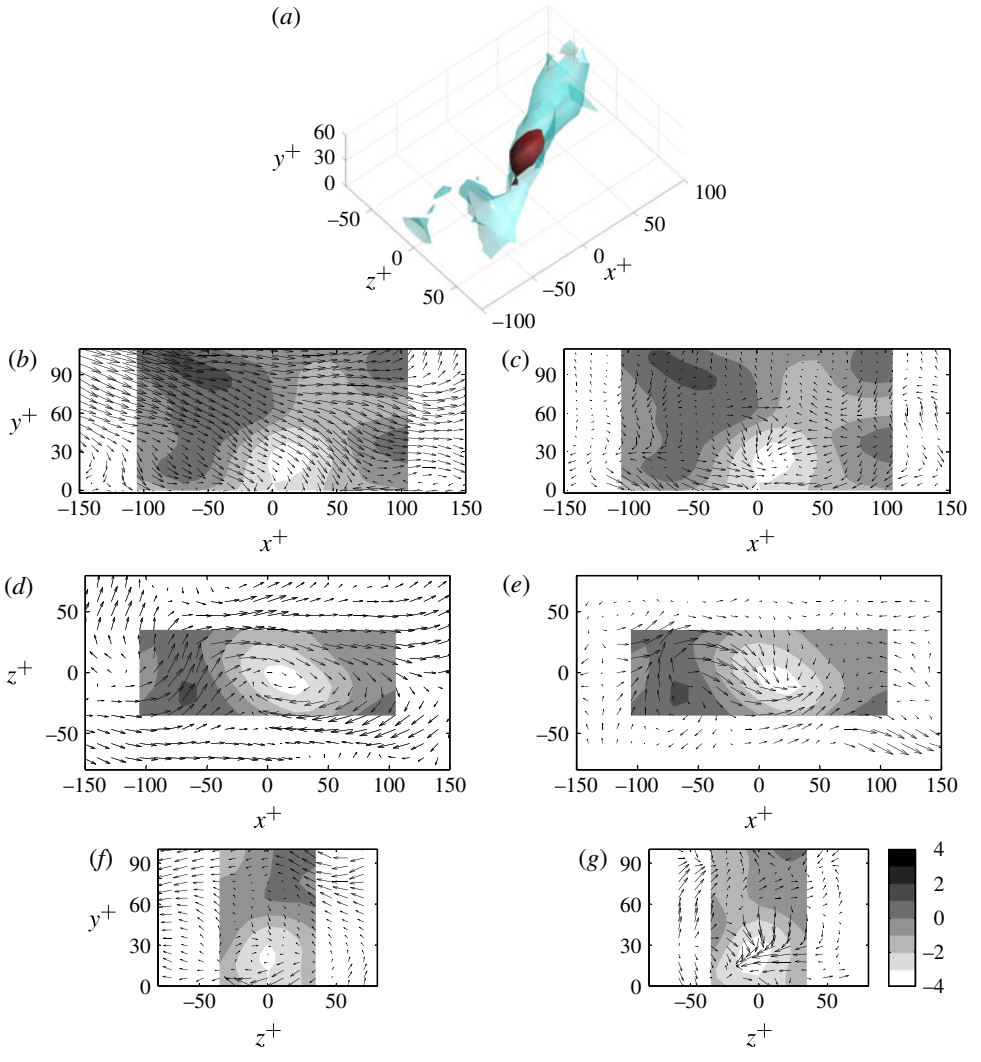

FIGURE 17. (Colour online) (*a*) An instantaneous visualization of a quasi-streamwise vortex identified by $Q = 0.5 \times 10^6$ s^{-2} embedding an isosurface of negative HAPP at $p_n = -3$. The velocity vector fields with background isocontour of pressure over planes (*b*) *xy*, (*d*) *xz*, and (*f*) *yz*. The material derivative $(\mathrm{D}U/\mathrm{D}t, \mathrm{D}V/\mathrm{D}t, \mathrm{D}W/\mathrm{D}t)$ vector obtained using the Lagrangian method with background isocontours of pressure over planes (*c*) *xy*, (*e*) *xz*, and (*g*) *yz*. The *xz*-plane crosses at $y^+ = 20$ and the *yz*-plane crosses at $x^+ = 0$.

seems to be a negative pressure blob partially captured at $x^+ = 100$. Each pair of successive positive and negative HAPPs appears to belong to a hairpin vortex in which the upstream shear layer forms the positive pressure and the spanwise vortex core forms the negative pressure region. The spanwise section of the hairpin vortices is observed at $x^+ = 0$ and 110 on figure 18(*b*). The downstream hairpin vortex is also larger since the centre of the positive-pressure region appears at a larger wall-normal distance. The succession of these two hairpin vortices and the increase of their size along the downstream direction suggests that they form a hairpin packet and as a result the succession of positive and negative HAPPs. This alternating behaviour of positive

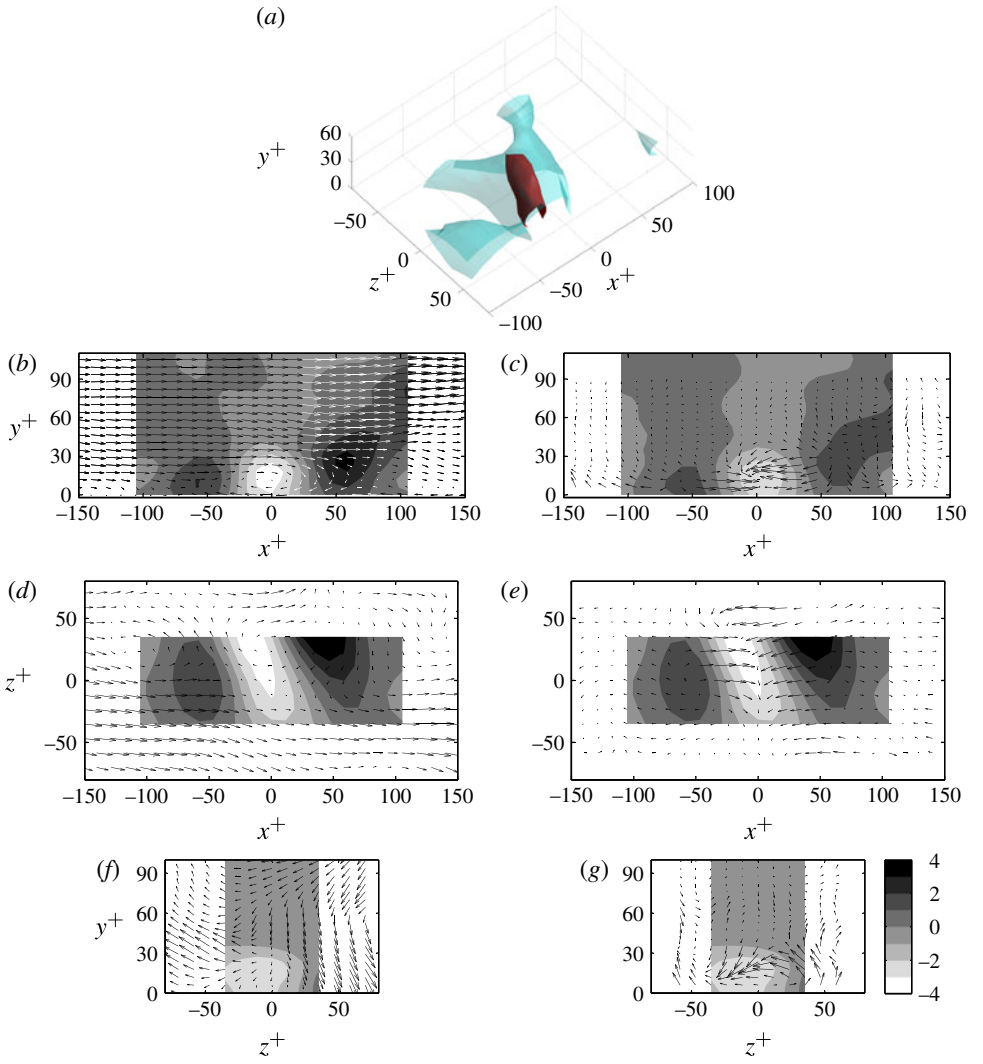

FIGURE 18. (Colour online) (*a*) An instantaneous visualization of a spanwise vortex identified by $Q = 0.5 \times 10^6\ \mathrm{s}^{-2}$ embedding an isosurface of negative HAPP at $p_n = -3$. The velocity vector fields with background isocontour of pressure over planes (*b*) *xy*, (*d*) *xz*, and (*f*) *yz*. The material derivative $(\mathrm{D}U/\mathrm{D}t, \mathrm{D}V/\mathrm{D}t, \mathrm{D}W/\mathrm{D}t)$ vector obtained using the Lagrangian method with background isocontours of pressure over planes (*c*) *xy*, (*e*) *xz*, and (*g*) *yz*. The *xz*-plane crosses at $y^+ = 20$ and the *yz*-plane crosses at $x^+ = 0$.

and negative HAPPs has also been noted in the previous literature (Schewe 1983; Ghaemi *et al.* 2012).

6. Turbulent structure of HAPPs

In this section, statistical analysis of the HAPPs is carried out to identify their turbulent structure. Conditional averaging of the velocity, pressure and turbulent quantities are investigated to identify the contribution of different structures and mechanisms to the formation of the HAPPs.

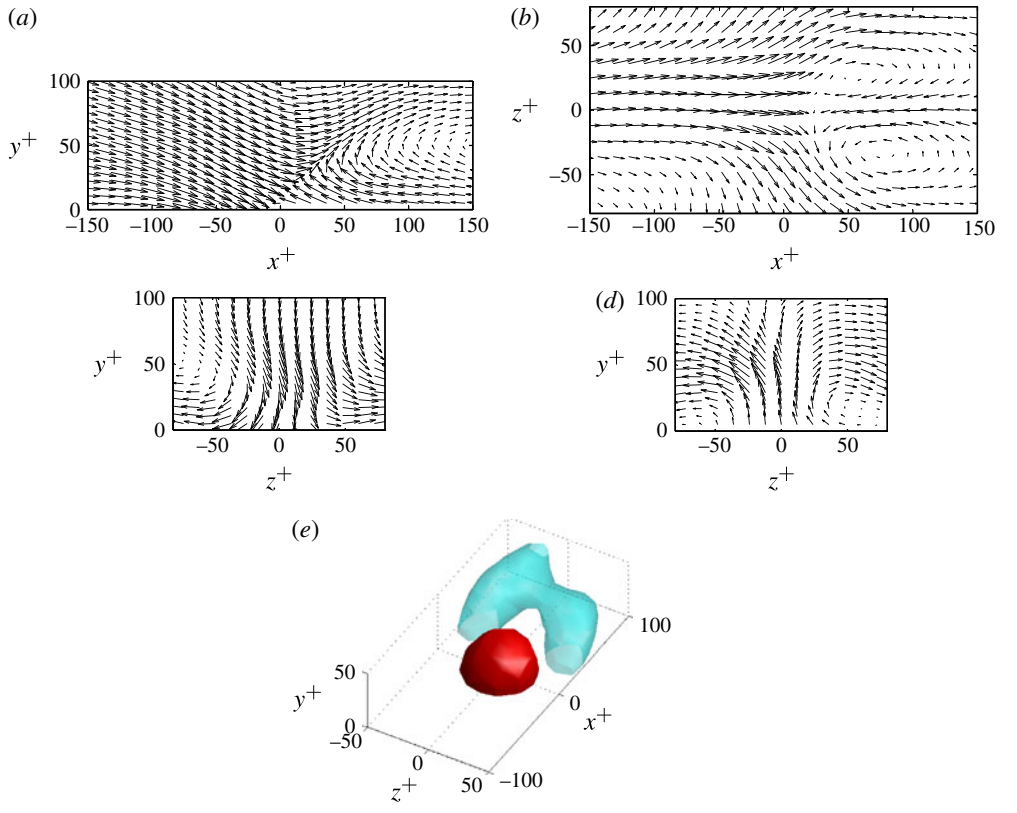

FIGURE 19. (Colour online) The conditional average of fluctuating velocity conditioned based on the positive HAPP showing the vector fields of fluctuating velocity in planes (*a*) *xy*, (*b*) *xz* (crossing at $y^+ = 20$), and *yz*-planes crossing at (*c*) $x^+ = -50$ and (*d*) $x^+ = +50$. (*e*) The three-dimensional vortex organization visualized by an isosurface of $Q = 0.8 \times 10^4\ \mathrm{s}^{-2}$ applied to the fluctuating velocity field (pale grey, blue online) along with the pressure fluctuation at $p_n = 1.5$ visualized using the dark isosurface (red online).

6.1. *Positive HAPPs*

The conditional average of the velocity fluctuations based on the positive HAPPs demonstrates a clear indication of shear layers detected by strong $\partial u/\partial x$ and $\partial u/\partial y$ as observed in figure 19(*a*). The average shear layer is formed between the upstream sweep of high-speed flow and the ejection event induced by a coherent vortex pattern. The origin of the sweep event appears to be beyond the inner layer as it exceeds $y^+ = 100$. The ejection event is induced by a hairpin vortex indicated by a spanwise core (hairpin head) at about $(x^+, y^+, z^+) = (130, 50, 0)$. The shear layer is inclined at an angle of 45° with respect to x which is in agreement with the estimation of Liu *et al.* (1991) for the shear layers at $y^+ < 100$ and also Adrian *et al.* (2000). However, it is larger than the 25° observed in the conditional averages of Johansson, Alfredsson & Kim (1991) and the inclination angle reported by the visualization of Klewicki & Hirschi (2004). The average shear layer also demonstrates a significant $\partial u/\partial z$ component in the *xz*-plane of figure 19(*b*). The wall-normal swirls of the two counter-rotating quasi-streamwise vortices of the hairpins are observed at $(x^+, y^+, z^+) = (80, 20, \pm 40)$ of the *xz*-plane. The upstream sweep of the flow towards

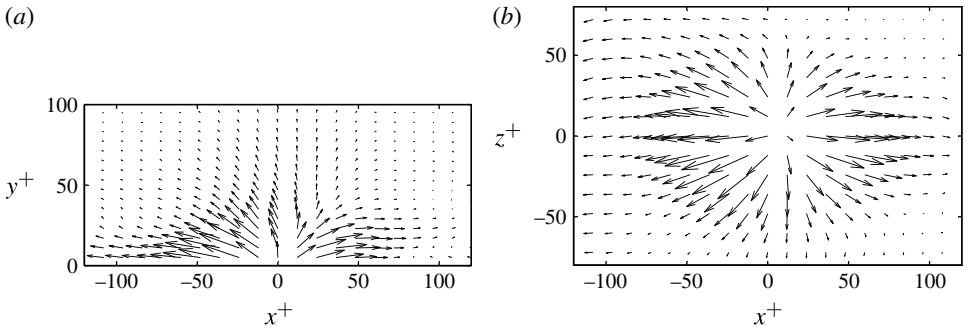

FIGURE 20. The conditional average of Lagrangian acceleration conditioned based on the positive HAPP in planes (*a*) *xy* and (*b*) *xz*, crossing at $y^+ = 20$.

the wall and the swirl of the quasi-streamwise vortices are also observed in the *yz* vector fields of figure 19(*c,d*), respectively. The three-dimensional organization of the hairpin vortex is illustrated in figure 19(*e*) with respect to the upstream positive HAPP. The two quasi-streamwise sections along with the spanwise part of the hairpin vortex induce the ejection event which has a major role in the formation of the shear layer.

The conditional average of figure 19 does not necessitate the existence of a complete hairpin vortex in the instantaneous realizations. As has been observed for the instantaneous visualization of figure 16, incomplete hairpin vortices (derivatives of hairpins according to Adrian 2007) may also form an ejection event and consequently a shear layer contributing to the formation of the positive HAPPs. For example, cane-type vortices which are formed by a quasi-streamwise and a spanwise vortex element (figure 10 of Ghaemi & Scarano 2011) contribute to the conditional-average pair of counter-rotating vortices. Therefore, the conceptual model of a hairpin vortex, which may include a complete or an incomplete hairpin vortex, is directly linked to the formation of positive HAPPs. The hairpin vortex produces the ejection event on its inboard region followed by the formation of the upstream shear layer and the stagnation point of positive HAPP.

The average flow field undergoes deceleration in all radial directions towards the centre of the positive HAPP as shown in the *xy*- and *xz*-planes of the material derivative in figure 20. The radial symmetry of the acceleration field is an interesting feature which is not apparent in the average fluctuation velocity fields of figure 19. In order to identify the contribution of the average velocity pattern to the material acceleration, the advection part ($\boldsymbol{U} \cdot \boldsymbol{\nabla U}$) of the material acceleration is shown in figure 21. It is observed that the average velocity pattern of the shear layer contributes to the streamwise and wall-normal components of decelerations in the sweep region upstream of the shear layer. However, the deceleration of the material derivative in the ejection region of figure 20 is not observed in the advection acceleration field of figure 21. This indicates that the sweep event has a longer lifetime and is advected with negligible change relative to the ejection event, while the ejection event causes temporal acceleration ($\partial \boldsymbol{U}/\partial t$) of the flow which is consistent with the 'burst' nature of these events defined as 'temporally intermittent eruption' of the fluid away from the wall by Robinson (1991). The advection acceleration also does not contribute to the symmetric spanwise acceleration observed in figure 20(*b*), indicating that the spanwise component is also generated by the temporal acceleration. The significant contribution of the temporal acceleration ($\partial \boldsymbol{U}/\partial t$) to the spanwise component of

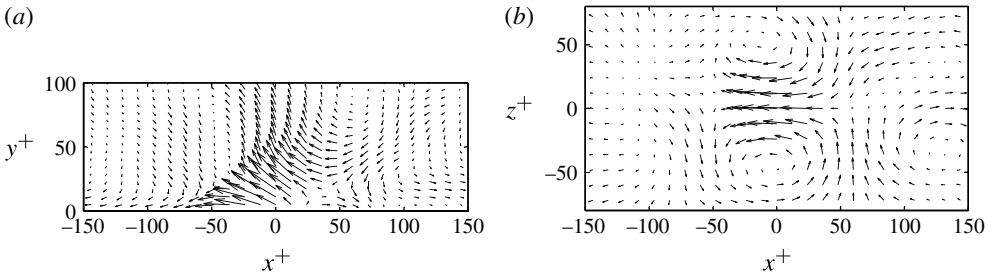

FIGURE 21. The conditional average of the advection part of the material acceleration ($\boldsymbol{U}\cdot\boldsymbol{\nabla U}$) based on positive HAPPs in planes (*a*) *xy* and (*b*) *xz*, crossing at $y^+ = 20$.

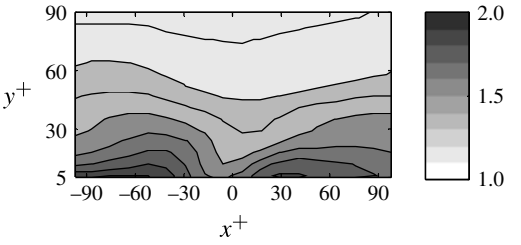

FIGURE 22. Non-dimensional turbulent kinetic energy per unit mass (k/u_τ^2) conditionally averaged based on positive HAPPs.

material acceleration ($\mathrm{D}U/\mathrm{D}t$) demonstrates that the asymmetry of the shear layer structures is associated with the burst event.

Shear layers and the corresponding burst events are considered the main mechanisms of turbulence production within the turbulent boundary layer (Kim *et al.* 1971; Johansson *et al.* 1991). The budget of turbulent kinetic energy is of interest to evaluate the contribution of different mechanisms, in particular the pressure transport of turbulent kinetic energy. The distribution of turbulent kinetic energy per unit mass $k = \langle u_i u_i/2\rangle$ illustrated in figure 22 demonstrates the overlap of the low-turbulent-kinetic-energy region with the stagnation region along the shear layer. The equation for the budget of turbulent kinetic energy is written as

$$\frac{\mathrm{D}k}{\mathrm{D}t} = -\langle u_i u_j\rangle \frac{\partial U_i}{\partial x_j} - \frac{\partial}{\partial x_i}\left[\frac{1}{2}\langle u_i u_j u_j\rangle\right] - \frac{1}{\rho}\frac{\partial}{\partial x_i}[\langle u_i p'\rangle] + \nu\frac{\partial^2}{\partial x_j \partial x_j}k - \nu\left\langle \frac{\partial u_i}{\partial x_j}\frac{\partial u_i}{\partial x_j}\right\rangle \quad (6.1)$$

[1] [2] [3] [4] [5] [6]

following Pope (2000). In this equation, term [1] is the material derivative of k, [2] is the turbulence production, [3] is turbulent transport of k, [4] is pressure transport, [5] is viscous diffusion, and [6] is the dissipation term. The equation can be simplified because the average of the conditional samples is theoretically steady and symmetric with respect to the *xy*-plane at $z^+ = 0$. The two spanwise halves of figure 19(*b*) in positive and negative z^+ regions show 16 % asymmetry evaluated as the r.m.s. of the velocity difference of the two halves normalized by the average velocity. Therefore,

the terms can be simplified for the conditional averages of the HAPP events as

$$[1] \qquad U\frac{\partial k}{\partial x} + V\frac{\partial k}{\partial y}, \tag{6.2}$$

$$[2] \qquad -\langle uv\rangle\frac{\partial U}{\partial y} - \langle uv\rangle\frac{\partial V}{\partial x} - \langle u^2\rangle\frac{\partial U}{\partial x} - \langle v^2\rangle\frac{\partial V}{\partial y}, \tag{6.3}$$

$$[3] \qquad -\frac{1}{2}\left[\frac{\partial}{\partial x}\langle u^3 + uv^2 + uw^2\rangle + \frac{\partial}{\partial y}\langle v^3 + vu^2 + vw^2\rangle\right], \tag{6.4}$$

$$[4] \qquad -\frac{1}{\rho}\left[\frac{\partial}{\partial x}\langle up\rangle + \frac{\partial}{\partial y}\langle vp\rangle\right], \tag{6.5}$$

$$[5] \qquad \nu\left[\frac{\partial^2 k}{\partial x^2} + \frac{\partial^2 k}{\partial y^2}\right], \tag{6.6}$$

$$[6] \quad -\nu\left\langle\left(\frac{\partial u}{\partial x}\right)^2 + \left(\frac{\partial u}{\partial y}\right)^2 + \left(\frac{\partial u}{\partial z}\right)^2 + \left(\frac{\partial v}{\partial x}\right)^2 + \left(\frac{\partial v}{\partial y}\right)^2 + \left(\frac{\partial v}{\partial z}\right)^2 + \left(\frac{\partial w}{\partial x}\right)^2 + \left(\frac{\partial w}{\partial y}\right)^2 + \left(\frac{\partial w}{\partial z}\right)^2\right\rangle. \tag{6.7}$$

These terms are more extended than those of the ensemble average of unconditioned realizations of the turbulent boundary layer which is two-dimensional ($\partial/\partial x = \partial/\partial z = 0$). The contours of the first four terms at the symmetric xy-plane ($z^+ = 0$) estimated over the sampled positive HAPPs are shown in figure 23. It is observed that the advection term in figure 23(a) has minimum value along the shear layer. A negative contribution of the advection term is observed in the sweep region upstream of the shear layer which acts to reduce turbulent kinetic energy. The contribution of the first part of the advection term [1] is larger than the second part since $U \gg V$ in the conditional average of the positive HAPPs. Therefore, the negative advection is caused by the negative $\partial k/\partial x$ at the immediate upstream location of the shear layer. And also the positive advection of kinetic energy immediately downstream of the shear layer is formed due to the positive $\partial k/\partial x$.

The production of turbulence for the average of conditionally selected HAPP events consists of both shear (the first two terms in [2]) and dilation (the last two terms in [2]) terms which includes three extra terms in comparison to that of the mean turbulent boundary layer (two-dimensional steady). The contours of figure 23(b) shows an inclined concentration of turbulence production along the shear layer while the peak is in the vicinity of the wall. It is expected that the mean shear (i.e. $\partial U/\partial x$, $\partial V/\partial x$, $\partial U/\partial y$, $\partial V/\partial y$) will make a major contribution to the turbulence production along the shear layer while the average correlation of the velocity fluctuations (i.e. $\langle uv\rangle$, $\langle u^2\rangle$, $\langle v^2\rangle$) forms the turbulence production in the upstream and downstream regions of the shear layer. The turbulent transport of kinetic energy in figure 23(c) shows a positive contribution along with an inclined pattern overlapping with the shear layer structure.

A strong positive contribution to the turbulent kinetic energy is observed from the pressure transport term along the shear layer in figure 23(d). Two regions with relatively weak negative contribution are also observed on both upstream and downstream sides of the shear layer. The high contribution of the pressure transport term to the budget of turbulent kinetic energy is in contrast to the unconditioned turbulent boundary layer. The pressure transport term within the inner layer of a turbulent boundary layer makes less than 1 % contribution to the budget of

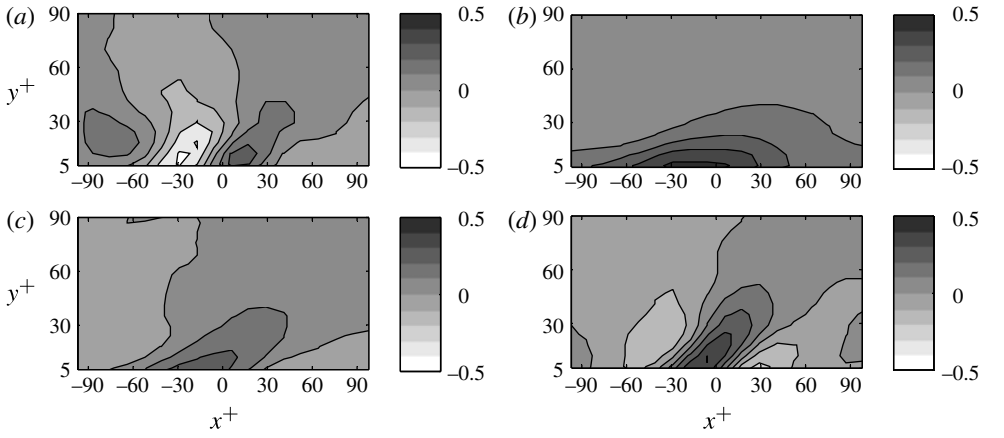

FIGURE 23. The budget of turbulent kinetic energy for the conditional average of positive HAPPs. (*a*) The advection of the kinetic energy, (*b*) the production of turbulence, (*c*) turbulent transport and (*d*) the pressure transport term in the *xy*-plane crossing at $z^+ = 0$. All the terms are non-dimensionalized using inner scales.

turbulent kinetic energy beyond a wall-normal distance of $y^+ = 10$ (Spalart (1988) at $Re_\theta = 1410$). The DNS of Spalart (1988) shows that the peak of the pressure transport term occurs at about $y^+ = 2$ which is ∼8 % of maximum turbulence production at $y^+ = 10$. However, the contribution of the pressure transport term to the budget of turbulent kinetic energy within the shear layers is comparable to the production term (95 % of the peak ratio). The positive contribution from the production term, the pressure term and also the turbulent transport should be balanced by the viscous diffusion and the dissipation terms to result in the negligible convection of turbulence observed along the shear layer.

6.2. *Negative HAPPs*

The average of the fluctuating velocity field conditioned based on the negative HAPPs (equation (2.5)) is demonstrated in figure 24. The average field in the *xy*-plane shows a vortex pattern with negative spanwise rotation accompanied by an ejection upstream and a sweep motion downstream of the vortex core. The vortex core at $x^+ = 0$ is observed to extend from the wall up to $y^+ = 25$ which is an artifact of averaging of vortices at different wall-normal heights. This pattern suggests that the spanwise vortices with the swirling centre located at wall-normal distances up to $y^+ = 25$ contribute to the negative HAPPs selected using the $-2p_{rms}$ threshold. The vortex is observed to be coherent over ∼50λ in the spanwise direction as observed in the *xz*-plane of figure 24(*b*). There is also a slight asymmetry observed due to low statistical convergence of the data in regions away from the centre of the HAPP. The velocity field within the *yz*-plane crossing at $x^+ = -50$ in figure 24(*c*) shows two counter-rotating streamwise vortices inducing a focused ejection event. The counter-rotating vortices are located upstream of the negative HAPP region and ∼100λ apart from each other. This pattern is similar to the hairpin vortex observed in the conditional average of figure 19 suggesting a close link between the hairpin vortices and the negative HAPPs. The sweep motion in the *yz*-plane at $x^+ = 50$ in figure 24(*d*) is associated with the downstream downwash of the spanwise vortex (Adrian 2007; Ghaemi *et al.*

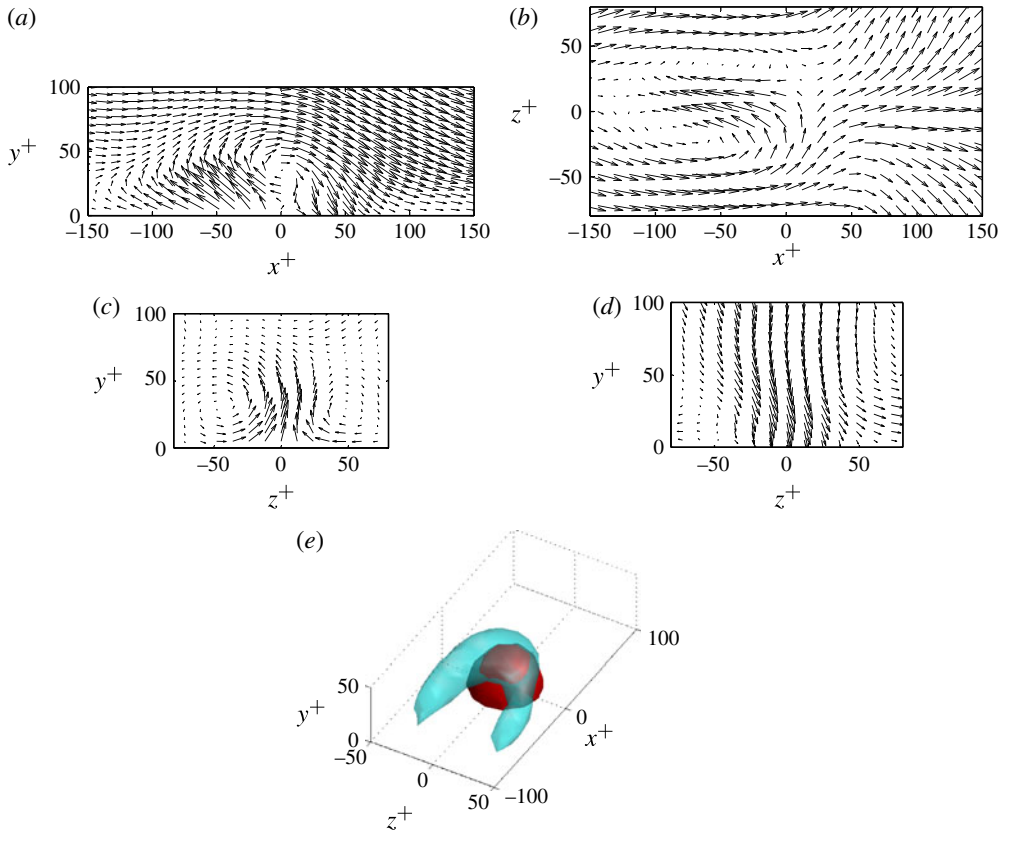

FIGURE 24. (Colour online) The conditional average of fluctuating velocity conditioned based on the negative HAPP showing vector fields of fluctuating velocity in planes (*a*) *xy*, (*b*) *xz* (crossing at $y^+ = 20$), and *yz*-planes crossing at (*c*) $x^+ = -50$ and (*d*) $x^+ = +50$. (*e*) The three-dimensional vortex organization visualized by the pale grey (blue online) isosurface of $Q = 0.8 \times 10^4\ \mathrm{s}^{-2}$ applied to the fluctuating velocity field along with pressure fluctuation at $p_n = -1.5$ visualized using the dark (red online) isosurface.

2012). The three-dimensional hairpin vortex pattern is also illustrated in figure 24(*e*) using the *Q*-criterion applied to the fluctuating velocity field.

Although a similar vortex pattern is observed in the conditional average of figures 19 and 24, the underlying mechanisms are different due to the location of the hairpin vortex relative to the centre of the HAPP. The hairpin vortex of figure 24 indicates strong correspondence of the negative HAPPs to the spanwise portion of the hairpin vortex as it is formed exactly above it. The other distinguishing feature is the lower statistical convergence of figure 24 even though the number of conditionally sampled negative HAPPs is higher than the positive ones. This is in particular observed in the *xz*-plane of figure 24(*b*) relative to figure 19(*b*) in which some degree of asymmetry and also ambiguity of the vortex cores are observed. The lower convergence rate could be due to the existence of other structures or vortices with different orientations in the conditionally sampled data. A structure which is suggested based on instantaneous observations similar to figure 17 is the quasi-streamwise vortices. These vortices can have both positive and negative streamwise/wall-normal

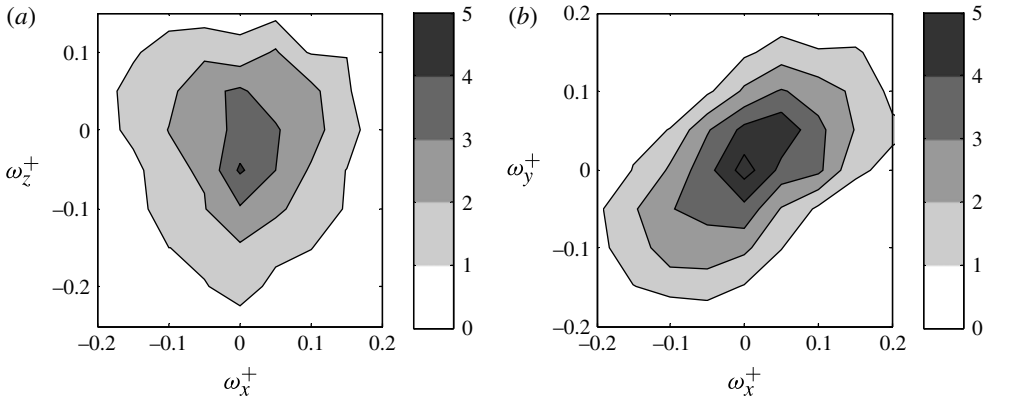

FIGURE 25. Contours of the joint probability density function of (*a*) ω_z^+ and ω_x^+ at $y^+ = 20$ and (*b*) ω_y^+ and ω_x^+ at $z^+ = 20$ of the conditional average of negative HAPPs.

vorticity and should smear out in the average field if full statistical convergence is achieved.

In order to study the orientation of the vortices forming the negative HAPPs joint probability density functions (j.p.d.f.) of (ω_x^+, ω_y^+) and (ω_x^+, ω_z^+) components of the vorticity vector within the conditional database of negative HAPPs are illustrated in figure 25. The combination of large negative ω_z^+ along with small values of ω_x^+ in figure 25(*a*) indicates the contribution of spanwise vortices rotating with the mean shear of the turbulent boundary layer. As shown in figure 26, the vortices with dominant ω_z^+ component form the spanwise portion of the hairpin category of vortices. The spanwise vortices may also have a slight streamwise (ω_x^+) or wall-normal (ω_y^+) inclination as observed in figure 25(*b*). The j.p.d.f. also demonstrates the contribution of two types of quasi-streamwise vortices with $\omega_x^+ > 0$ and $\omega_z^+ > 0$ or with the opposite direction which is characterized as $\omega_x^+ < 0$ and $\omega_z^+ < 0$. As shown in figure 26, these two orientations of streamwise vortices are associated with the counter-rotating quasi-streamwise vortices which can also be the leg of a hairpin vortex. The analysis demonstrates that both spanwise and quasi-streamwise vortices contribute to the formation of the negative HAPPs in the turbulent boundary layer.

The relative contribution of hairpins (spanwise-dominated vortices) or quasi-streamwise vortices to the formation of the negative HAPPs can be estimated based on a set of thresholds. The p.d.f. of figure 25(*a*) indicates that ∼25 % of the vortices are hairpins, assuming that a hairpin vortex is characterized as a vortex with dominant spanwise orientation with $\omega_z^+ < 0$ and $|\omega_x^+| < 0.05$. The quasi-streamwise vortices also form ∼60 % of the distribution if they are characterized by $|\omega_x^+| < 0.05$. However, it is important to note that the detected quasi-streamwise vortices may also be connected to a spanwise portion and therefore form a hairpin vortex.

The conditional average of fluid acceleration ($\mathrm{D}U/\mathrm{D}t$) over the negative HAPPs in figure 27 demonstrates symmetric acceleration of the fluid towards the centre of the plot (pressure minima) from all radial directions. This pattern is similar to the acceleration field of figure 20 but in the reverse direction. The major wall-normal component of acceleration towards the centre is due to the advection acceleration ($\boldsymbol{U} \cdot \boldsymbol{\nabla} \boldsymbol{U}$) as shown in figure 28. The comparison of the two figures suggests that

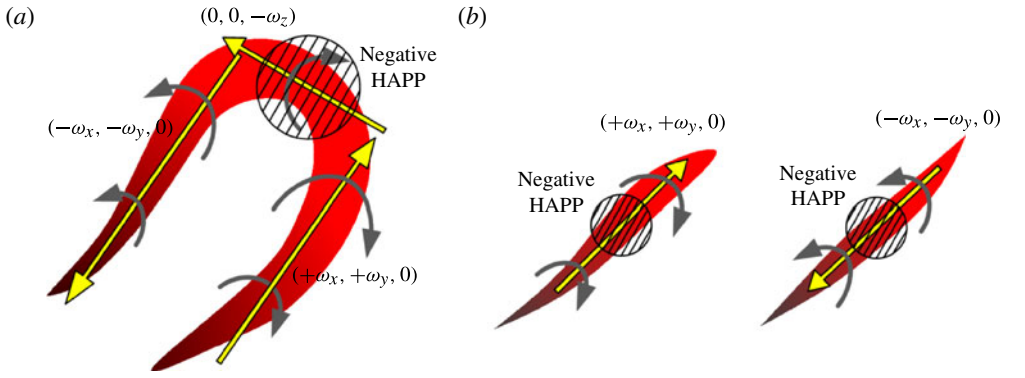

FIGURE 26. (Colour online) (*a*) A hairpin vortex and (*b*) two counter-rotating quasi-streamwise vortices. The quasi-streamwise vortices in (*b*) may also be considered as the derivatives of the hairpin vortex.

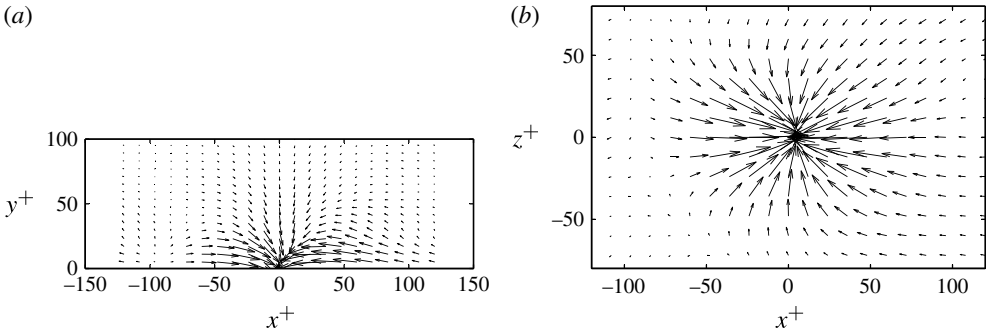

FIGURE 27. The conditional average of Lagrangian acceleration conditioned based on negative HAPPs in planes (*a*) *xy* and (*b*) *xz* at $y^+ = 20$.

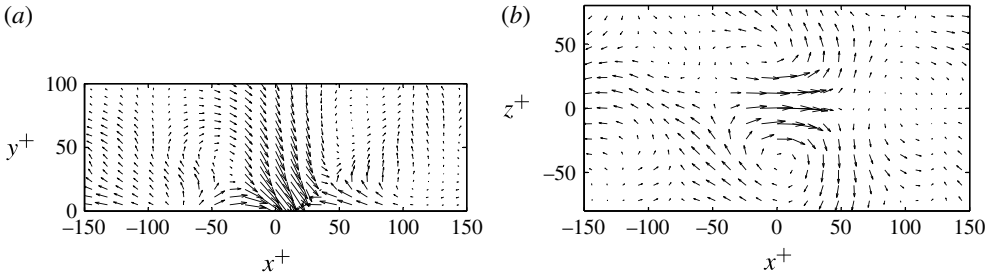

FIGURE 28. The conditional average of the advection part of the material acceleration $(\boldsymbol{U} \cdot \boldsymbol{\nabla} \boldsymbol{U})$ based on negative HAPPs in planes (*a*) *xy* and (*b*) *xz* at $y^+ = 20$.

temporal acceleration $(\partial \boldsymbol{U}/\partial t)$ contributes to the streamwise component and also significantly to the spanwise component.

The investigation of the instantaneous visualizations of § 5.3 and the conditional averages of this section show that two types of vortices are dominantly involved in the

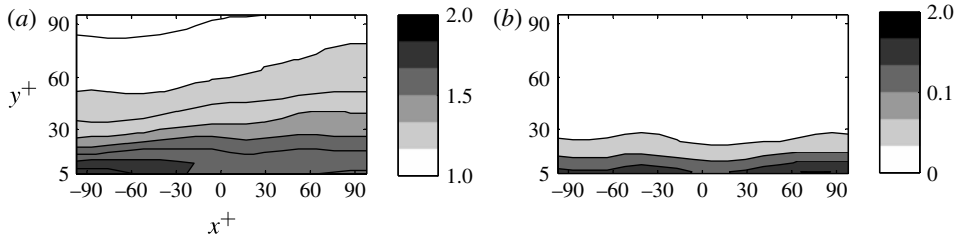

FIGURE 29. (*a*) Non-dimensional turbulent kinetic energy per unit mass k/u_τ^2 and (*b*) the production of turbulence (term [3] of (6.1)) conditionally averaged based on the negative HAPPs.

formation of negative HAPPs: (*a*) the spanwise or streamwise section of a hairpin vortex and (*b*) the quasi-streamwise vortices. Although isolated quasi-streamwise vortices which appear in the inner layer of the turbulent boundary layer are commonly considered as individual coherent structures (Guezennec, Piomelli & Kim 1989; Sheng *et al.* 2009), they may also be considered as a part of the hairpin category of vortices (Adrian 2007). These vortices along with the orientation of the vorticity vector are shown in figure 26.

The turbulent kinetic energy of the conditionally sampled negative HAPPs is shown in figure 29(*a*) demonstrating a small region of higher turbulent kinetic energy between $x^+ = -90$ and -30 which corresponds to the ejection region upstream of the spanwise vortex core observed in figure 24(*a*). The analysis of the budget of the turbulent kinetic energy of the negative HAPPs shows that the advection, turbulent and pressure transport terms are negligible as they are an order of magnitude smaller than those of the positive HAPPs. The only considerable term is the production of turbulence which is shown in figure 29(*b*). The region of the vortex core at $x^+ = 0$ appears to result in the local minimum of the turbulence production. The turbulence production term is expected to be balanced by viscous diffusion and dissipation terms.

6.3. *The HAPPs and the hairpin paradigm*

The analysis demonstrated that the shear layer is the source of the positive HAPPs and the core of the vortical structures (streamwise or spanwise) is the source of the negative HAPPs. These turbulent sources are dominant coherent structures of the turbulent boundary layer which are included in the hairpin vortex paradigm. In this conceptual model, the shear layer is present in the region upstream of the hairpin vortex where the ejection event opposes the incoming flow. The vortices with spanwise and quasi-streamwise orientation are also associated with the head and the legs of the hairpin vortex, respectively. Therefore, a reverse analysis to that of §§ 6.1 and 6.2 is expected to demonstrate their association with the HAPPs upon sampling the hairpin vortices.

The sampling procedure based on the detection of hairpin vortices using ejection events as described in § 2.6 followed by averaging of both the velocity and the pressure field results in the three-dimensional visualization of figure 30. An upstream region of positive pressure is observed which corresponds to the shear layer region. There is also a negative-pressure region overlapping with the spanwise (head) and the quasi-streamwise (neck) region of the hairpin vortex. The vortex organization demonstrates a hairpin vortex with an increase of inclination angle from $\sim 10°$ at $y^+ = 25$ to $25°$ at $y^+ = 75$. The level of the pressure isosurfaces ($p_n = \pm 0.3$) is

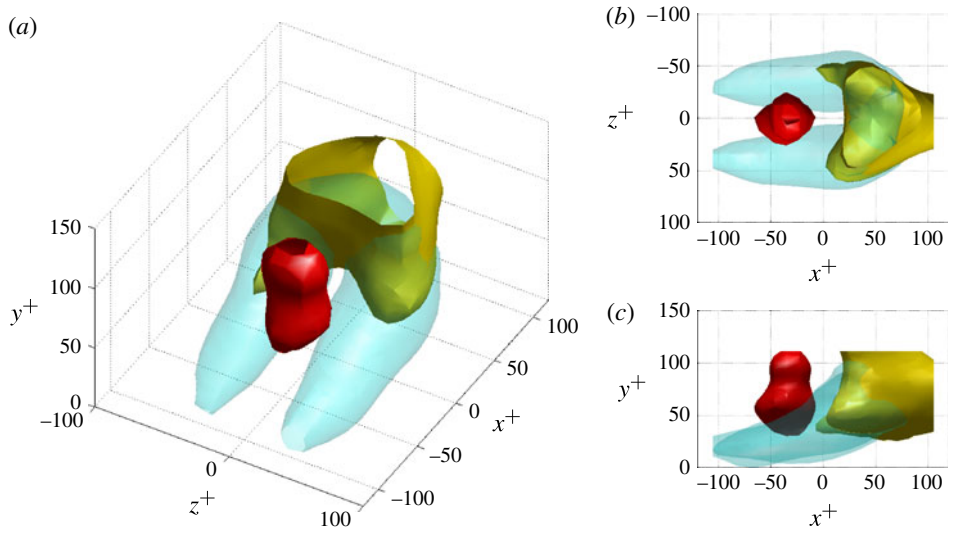

FIGURE 30. (Colour online) Conditional average of the pressure field and the velocity field based on the detection of ejection events ($u < 0$ and $v > 0$) with the threshold of $uv/U_\infty^2 < -0.025$. (*a*) Three-dimensional view and (*b,c*) x, y- and x, z-planes. The transparent blue (light grey) isocontours visualizes the vortex at $Q = 0.3 \times 10^5$ s^{-2} while the red blob (dark grey at upstream) and the yellow blob (medium grey at downstream) isosurfaces identify positive and negative pressure fluctuations at $p_n = 0.3$ and -0.3, respectively.

lower than the threshold used in the previous analysis for the detection of the HAPPs ($p_n = \pm 2$). This is partly due to the jitter in the conditional data resulting in lower levels of average pressure field. More important, it shows that not all the hairpins contain two HAPPs and the analysis does not prove a bi-directional relation between the HAPPs and the hairpins. However, a consideration of the pressure peaks in the conditional averages demonstrates the role of the hairpin vortex model in the generation of successive positive and negative high-amplitude pressure peaks within the turbulent boundary layer.

7. Discussion

The current investigation associates the turbulent structure of the positive HAPPs with the shear layers of the turbulent boundary layer, which is evident in both instantaneous visualizations and also the conditional averages of the velocity field. The visualizations demonstrate a high-pressure region overlapping with a shear layer structure formed by the interaction of an upstream sweep event and a downstream ejection event. The sweep event appears to initiate from the outer layer while the ejection event is formed by the hairpin category of vortices within the inner layer. Although a complete hairpin vortex is infrequent in the instantaneous visualizations, the conditional average shows strong evidence of a hairpin vortex immediately downstream of the shear layer.

The comparison with the previous investigations shows that the result agrees with the experimental study of Johansson *et al.* (1987) while it contradicts Kim *et al.* (2002). The positive HAPPs were linked to the sweep motion of an upstream pair of counter-rotating streamwise vortices by Kim *et al.* (2002) which may be due to

their analysis at a single location 20λ upstream of the pressure event. The upstream location was selected due to the observed high correlation between wall pressure and streamwise vorticity but this does not necessarily indicate the focus of the involved turbulent structure. The association of the positive pressure fluctuations of the turbulent boundary layer (not necessarily the HAPPs) with the shear layer was also observed by Johansson *et al.* (1991) and discussed by Robinson (1991).

The conditional average of the advection acceleration showed that the sweep event upstream of the shear layer has a passive role as it is advected with small changes in its spatial structure. On the other hand, the ejection event (burst) has intermittent behaviour causing temporal acceleration of the field in the streamwise and spanwise directions. As a result, the spanwise acceleration and the asymmetry of the shear layer structures, which are also emphasized by Johansson *et al.* (1991), are related to the ejection event downstream of the shear layer. The results allow extension of the hypothesis of Johansson *et al.* (1991) on the reduction of turbulence production by inhibition of the asymmetric behaviour of the shear layers. It is conjectured that control of the ejection events which are produced by local instability of the low-speed streaks would be effective in generating symmetric shear layers and the final reduction of turbulence production.

The association of the negative HAPPs with both spanwise and streamwise vortical structures of the turbulent boundary layer has been observed in the instantaneous visualizations and also in the joint probability analysis of vorticity components. The conditional averages of the velocity field show evidence of the spanwise vortices in the formation of negative HAPPs while the quasi-streamwise vortices smear out in the averaging procedure. The results agree neither with the conclusion of Johansson *et al.* (1987) nor with Kim *et al.* (2002). However, they follow the conjecture of Robinson (1991) who related negative pressure fluctuations of the turbulent boundary layer to the core of the vortical structures. According to the current investigation, the core of the vortical structure could be the spanwise or the streamwise section of a hairpin vortex or it may belong to an isolated streamwise vortex.

The investigation of Johansson *et al.* (1987) based on the conditional average of the fluctuating velocity components (u and v) showed a positive peak in u and a negative peak in v (in time domain) and consequently associated the negative HAPPs with sweep-type events. Scrutiny of their investigation method shows that the detection of the HAPPs was based on exceeding a certain threshold (less than $2.5p_{rms}$) while it should have been based on detection of local minima events. This has resulted in high jitter and smearing of the conditional averages. Johansson *et al.* (1987) attempted to attenuate the jitter using an iterative alignment method based on cross-correlation between the conditioned signals and the averaged signal which indeed improved the average velocity field and showed a positive fluctuation of u followed by a weak negative fluctuation. However, they have only applied the procedure to a single wall-normal location at $y^+ = 15$ (figure 19 of Johansson *et al.* 1987) and did not perceive the vortex pattern. Although the turbulent structure proposed by Kim *et al.* (2002) does not agree with the current study, their observed flow pattern, which is an upstream ejection of the flow by a pair of counter-rotating vortices, is observed in figure 24 of this study.

The negative skewness factor of the wall pressure indicates a higher number of negative HAPPs than positive ones. This is also physically expected since according to the analysis each hairpin vortex may only introduce one positive HAPP as there is only one shear layer upstream of it. On the other hand, each of the two legs (quasi-streamwise vortices) or the head (spanwise vortex) may introduce an isolated

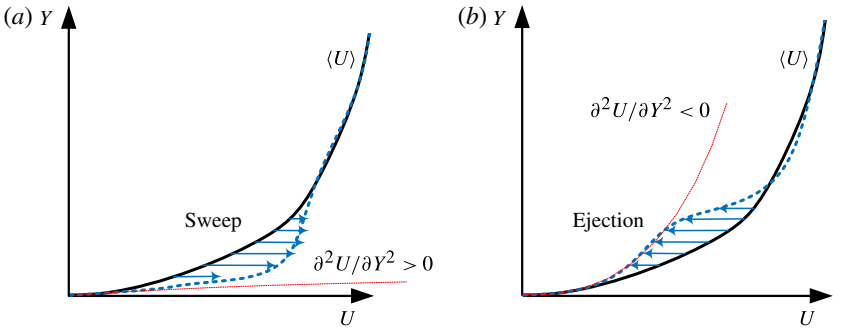

FIGURE 31. (Colour online) The curvature ($\partial^2 U/\partial Y^2$) of the velocity profile during sweep and ejection events. (*a*) The sweep event causing positive curvature and (*b*) the ejection event intensifying the negative curvature of the average velocity profile.

negative HAPP if there is a complete hairpin vortex. However, in practice due to the existence of isolated quasi-streamwise vortices, incomplete hairpins, and weak vortices, the number of negative HAPPs is only slightly higher than the positive HAPPs.

High-amplitude events which are a few times larger than the r.m.s. of the signal are not only limited to the wall pressure. This intermittent behaviour is also evident in the high values of kurtosis factor (k) in the near-wall velocity fluctuation and the wall shear stress (τ_w). The DNS of Kim *et al.* (1987) and Eggels *et al.* (1994) show intermittency of streamwise velocity in the immediate vicinity of the wall with kurtosis factor of $k \simeq 4$ and 5.3, respectively. Alfredsson *et al.* (1988*b*) also measured $k = 5$–6.5 for the streamwise velocity at $y^+ = 1$ within at a wide range of Reynolds numbers in different flow facilities. Chew, Khoo & Li (1994) measured $k = 5.2$ at $y^+ = 2.2$ for the wall shear stress in the viscous sublayer of a turbulent boundary layer. Although the agreement between different experimental or numerical works on the exact value of k is rather poor, the large values of k indicate intermittency and the existence of high-amplitude peaks in the velocity or wall shear stress signals similar to the HAPPs of the wall pressure.

The relation between the instantaneous wall pressure and the flow events of the velocity field immediately above the wall is depicted through the momentum equation evaluated at the wall surface as

$$\frac{\partial P}{\partial X} = \mu \frac{\partial^2 U}{\partial Y^2}. \tag{7.1}$$

This equation can be interpreted by considering the negative streamwise pressure gradient $\langle \partial P/\partial x \rangle$ as the driving mechanism of a turbulent flow over the wall surface causing negative $\langle \partial^2 U/\partial y^2 \rangle$ (curvature) of the average velocity profile. In the current experiment, the average velocity profile results in $\langle \partial P/\partial x \rangle \simeq -0.1$ Pa m^{-1}, equivalent to a negligible pressure change of $0.0002 p_{rms}$ (0.1 mPa) over 26λ (1 mm) distance. Therefore, the instantaneous pressure and velocity field is dominated by the fluctuating components and in particular by the HAPPs reaching a few p_{rms}.

According to (7.1), a positive pressure gradient $\partial P/\partial X > 0$ is accompanied by a positive $\partial^2 U/\partial Y^2$ which necessitates change in the curvature of the instantaneous velocity profile relative to the average profile. The change is introduced by a sweep event causing an inflection point at the wall as shown in the schematic drawing of figure 31(*a*). The connection of the sweep event with positive pressure gradient agrees

with figures 19 and 24 in which the sweep events are present where $\partial P/\partial X$ is positive. The sweep region is also directly related to high shear stress at the wall since in the viscous sublayer close to the wall the shear stress is approximated as $\tau_w \approx \mu U/Y$. Therefore, the upstream region of the conditionally averaged velocity field of the positive HAPPs and the downstream region of the conditionally averaged negative HAPP are characterized by positive pressure gradient, a sweep of flow toward the wall, and high wall shear stress. The sweep event initiating from the outer layer and its subsequent high-friction region upstream of the positive HAPP in figure 19 agrees well with the observation of Hutchins *et al.* (2011) in which the large-scale skin-friction events form the high-speed zones convecting with the local mean velocity of the logarithmic region.

The reverse mechanism regarding the negative pressure gradient $\partial P/\partial X < 0$ is associated with an ejection event as shown in the schematic drawing of figure 31(*b*). The ejection of fluid intensifies the negative curvature ($\partial^2 U/\partial Y^2 < 0$), exceeding that of the average velocity profile. The region of negative pressure gradient observed downstream of the positive HAPP in figure 19 and also upstream of the negative HAPP both show ejection events which also indicate a stress minimum region. Measurement of the exact value of shear stress and in particular the inflection point of the velocity profile is beyond the capabilities of the current experimental setup. This requires measurement with extremely high spatial resolution similar to Sheng *et al.* (2009) using digital holographic microscopy. In addition, the inflection point should be detected using the instantaneous velocity fields as it may smear out in the conditionally average field due to phase jitter.

The importance of the HAPPs in relation to the velocity field is further recognized by considering their association with both the hairpin paradigm (Adrian *et al.* 2000) and the superstructure events (Hutchins *et al.* 2011). The positive HAPP (shear layer) and the negative HAPP (vortical structures) are essential elements of the hairpin paradigm which are frequently observed in the boundary between large-scale zones of low and high momentum (Ganapathisubramani *et al.* 2012). In particular, the shear layer and the overlapping positive HAPP form the cross-over point between intensified small-scale fluctuations within the upstream high-momentum zone and the weakened small-scale fluctuations of the downstream zone (Hutchins *et al.* 2011).

8. Conclusion

The turbulent structure of HAPPs in a turbulent boundary layer was investigated using tomo-PIV. The measured time-resolved three-dimensional velocity fields of the inner layer are applied to evaluate the acceleration field using the Lagrangian method and followed by integration of the Poisson pressure equation to obtain the pressure field. The simultaneous volumetric velocity, acceleration, and pressure data are conditionally sampled based on local maxima and minima of wall pressure to analyse the three-dimensional turbulent structure of the HAPPs.

The analysis associated the positive HAPPs with the shear layer structures formed by an upstream sweep event opposing a downstream ejection event. The sweep event initiates from the outer layer while the ejection is formed by the hairpin category of vortices. The kinematics and dynamics of the shear layers are both asymmetric in the instantaneous visualizations of the velocity and acceleration fields. The asymmetric pattern originates from the strong spanwise component of temporal acceleration of the ejection event downstream of the shear layer. The analysis demonstrated a significant contribution of the pressure transport term to the budget of the turbulent kinetic energy

in the shear layers. The conditional averages and the orientation of the vortices showed that negative HAPPs are linked to both the spanwise and quasi-streamwise vortices of the turbulent boundary layer. Both of these vortices can be associated with the hairpin category of vortices while the isolated quasi-streamwise vortices also contribute to the negative HAPPs.

Acknowledgements

This work was conducted as a part of the FLOVIST project (Flow Visualization Inspired Aeroacoustics with Time Resolved Tomographic Particle Image Velocimetry) funded by the European Research Council (ERC), grant no 202887.

REFERENCES

ACALAR, M. S. & SMITH, C. R. 1987 A study of hairpin vortices in a laminar boundary layer. Part 2. Hairpin vortices generated by fluid injection. *J. Fluid Mech.* **175**, 43–83.

ADRIAN, R. J. 2007 Hairpin vortex organization in wall turbulence. *Phys. Fluids* **19**, 041301.

ADRIAN, R. J., MEINHART, C. D. & TOMKINS, C. D. 2000 Vortex organization in the outer region of the turbulent boundary layer. *J. Fluid Mech.* **422**, 1–54.

ALFREDSSON, P. H., JOHANSSON, A. V., HARITONIDIS, J. H. & ECKELMANN, H. 1988*a* The fluctuating wall-shear stress and the velocity field in the viscous sublayer. *Phys. Fluids* **31**, 1026–1033.

ALFREDSSON, P. H., JOHANSSON, A. V. & KIM, J. 1988*b* Turbulence production near walls: the role of flow structures with spanwise symmetry. In *Proceeding of the Summer Program*, pp. 131–141, Center for Turbulence research, Stanford, California.

ANDREOPOULOS, J. & AGUI, J. H. 1996 Wall-vorticity flux dynamics in two-dimensional turbulent boundary layer. *J. Fluid Mech.* **309**, 45–84.

ANTONIA, R. A. 1981 Conditional sampling in turbulence measurement. *Annu. Rev. Fluid Mech.* **13**, 131–156.

BAUR, T. & KÖNGETER, J. 1999 PIV with high temporal resolution for the determination of local pressure reductions from coherent turbulent phenomena. In *Proceedings of the 3rd International Workshop on Particle Image Velocimetry, Santa Barbara, USA*.

BLACKWELDER, R. F. & KAPLAN, R. E. 1976 On the wall structure of the turbulent boundary layer. *J. Fluid Mech.* **76**, 89.

BLAKE, W. K. 1970 Turbulent boundary-layer wall-pressure fluctuations on smooth and rough walls. *J. Fluid Mech.* **44**, 637.

BOILLOT, W. K. & PRASAD, A. K. 1996 Optimization procedure for pulse separation in cross-correlation PIV. *Exp. Fluids* **21**, 87–93.

BRADSHAW, P. 'Inactive' motion and pressure fluctuations in turbulent boundary layers. *J. Fluid Mech.* **30**, 241.

BROUWER, H. H. & RIENSTRA, S. W. 2008 Aeroacoustics research in Europe: the CEAS–ASC report on 2007 highlights. *J. Sound Vib.* **318**, 625–654.

BULL, M. K. 1967 Wall pressure fluctuations associated with subsonic turbulent boundary layer flow. *J. Fluid Mech.* **28**, 719.

CHANG, P. A. III, PIOMELLI, U. & BLAKE, W. K. 1999 Relationship between wall pressure and velocity-field sources. *Phys. Fluids* **11**, 3434–3448.

CHARONKO, J. J., KING, C. V., SMITH, B. L. & VLACHOS, P. P. 2010 Assessment of pressure field calculations from particle image velocimetry measurements. *Meas. Sci. Technol.* **21**, 105401.

CHEW, Y. T., KHOO, B. C. & LI, G. L. 1994 A time-resolved hot-wire shear stress probe for turbulent flow: use of laminar flow calibration. *Exp. Fluids* **17**, 75–83.

CHOI, K. S. 1989 Near-wall structure of a turbulent boundary layer with riblets. *J. Fluid Mech.* **208**, 417.

CLINCH, J. M. 1969 Measurement of the wall pressure field at the surface of a smooth-wall pipe containing turbulent water flow. *J. Sound Vib.* **9**, 398.

CORCOS, G. M. 1963 Resolution of pressure in turbulence. *J. Acoust. Soc. Am.* **35**, 192–199.

DAVIDSON, P. A. 2004 *Turbulence: An Introduction for Scientists and Engineers*. Oxford University Press.

DE KAT, R. & VAN OUDHEUSDEN, B. W. 2012 Instantaneous planar pressure determination from PIV in turbulent flow. *Exp. Fluids* **52**, 1089–1106.

DE OJEDA, W. & WARK, C. E. 1997 Instantaneous velocity and wall pressure features in a turbulent boundary layer. *Final Rep.* ONR N00014-93-1-0639.

EGGELS, J. G. M., UNGER, F., WEISS, M. H., WESTERWEEL, J., ADRIAN, R. J., FRIEDRICH, R. & NIEUWSTADT, F. T. M. 1994 Fully developed turbulent pipe flow: a comparison between direct numerical simulation and experiment. *J. Fluid Mech.* **268**, 175–209.

ELSINGA, G. E. 2008 Tomographic particle image velocimetry and its application to turbulent boundary layer, PhD thesis, Delft University of Technology.

FARABEE, T. M. & CASARELLA, M. J. 1991 Spectral features of wall pressure fluctuations beneath turbulent boundary layers. *Phys. Fluids* **3**, 2410.

FFOWCS WILLIAMS, J. E. & HALL, L. H. 1970 Aerodynamic sound generation by turbulent flow in the vicinity of a scattering half plane. *J. Fluid Mech.* **40**, 657.

GANAPATHISUBRAMANI, B., HUTCHINS, N., MONTY, J. P., CHUNG, D. & MARUSIC, I. 2012 Amplitude and frequency modulation in wall turbulence. *J. Fluid Mech.* **712**, 61–91.

GANAPATHISUBRAMANI, B., LONGMIRE, E. K. & MARUSIC, I. 2006 Experimental investigation of vortex properties in a turbulent boundary layer. *Phys. Fluids* **18**, 055105.

GHAEMI, S., RAGNI, D. & SCARANO, F. 2012 PIV-based pressure fluctuations in the turbulent boundary layer. *Exp. Fluids* **53** (6), 1823–1840.

GHAEMI, S. & SCARANO, F. 2010 Multi-pass light amplification for tomographic particle image velocimetry applications. *Meas. Sci. Technol.* **21** (12), 127002.

GHAEMI, S. & SCARANO, F. 2011 Counter-hairpin vortices in the turbulent wake of a sharp trailing-edge. *J. Fluid Mech.* **689**, 317–356.

GRAVANTE, S. P., NAGUIB, A. M., WARK, C. E. & NAGIB, H. M. 1998 Characterization of the pressure fluctuations under a fully developed turbulent boundary layer. *AIAA J.* **36** (10), 1808–1816.

GUEZENNEC, Y. G., PIOMELLI, U. & KIM, J. 1989 On the shape and dynamics of wall structures in turbulent channel flow. *Phys. Fluids* A **1** (4), 764–766.

GURKA, R., LIBERZON, A., HEFETZ, D., RUBINSTEIN, D. & SHAVIT, U. 1999 Computation of pressure distribution using PIV velocity data. In *Proceedings of the 3rd International Workshop on Particle Image Velocimetry, Santa Barbara, USA*.

HARITONIDIS, J. H., GRESKO, L. S. & BREUER, K. S. 1990 Wall pressure peaks and waves. In *Near-Wall Turbulence, Proceedings of the 1988 Zoran Zaric Memorial Conference* (ed. S. J. Kline & N. H. Afgan), pp. 397–417. Hemisphere.

HEAD, M. R. & BANDYOPADHYAY, P. 1981 New aspects of turbulent boundary-layer structure. *J. Fluid Mech.* **107**, 297–338.

HERMAN, G. T. & LENT, A. 1976 Iterative reconstruction algorithms. *Comput. Biol. Med.* **6**, 273–294.

HOWE, M. S. 1991 Surface pressures and sound produced by turbulent flow over smooth and rough walls. *J. Acoust. Soc. Am.* **90**, 1041.

HUNT, J. C. R., WRAY, A. A. & MOIN, P. 1988 Eddies, stream, and convergence zones in turbulent flows. *Research Rep.* CTR-S88, pp. 193–208. Center for Turbulence Research, Stanford.

HUSSAIN, A. K. M. F. & REYNOLDS, W. C. 1975 Measurements in fully developed turbulent channel flow. *J. Fluid Mech.* **97**, 568–578.

HUTCHINS, N., MONTY, J. P., GANAPATHISUBRAMANI, B., NG, H. C. H. & MARUSIC, I. 2011 Three-dimensional conditional structure of a high-Reynolds-number turbulent boundary layer. *J. Fluid Mech.* **673**, 255–285.

JEONG, J. & HUSSAIN, F. 1995 On the identification of a vortex. *J. Fluid Mech.* **285**, 69–94.

JOHANSSON, A. V. & ALFREDSSON, P. H. 1982 On the structure of turbulent channel flow. *J. Fluid Mech.* **122**, 295–314.

JOHANSSON, A. V., ALFREDSSON, P. H. & KIM, J. 1991 Evolution and dynamics of shear-layer structures in near-wall turbulence. *J. Fluid Mech.* **224**, 579–599.

JOHANSSON, A. V., HER, J. Y. & HARITONIDIS, J. H. 1987 On the generation of high-amplitude wall-pressure peaks in turbulent boundary layers and spots. *J. Fluid Mech.* **175**, 119.

KARANGELEN, C. C., WILCZYNSKI, V. & CASARELLA, M. J. 1993 Large amplitude wall pressure events beneath a turbulent boundary layer. *Trans. ASME: J. Fluids Engng* **115**, 653–659.

KIM, H. T., KLINE, S. J. & REYNOLDS, W. C. 1971 The production of turbulence near smooth wall in a turbulent boundary layer. *J. Fluid Mech.* **50**, 133–160.

KIM, J. 1983 On the structure of wall-bounded turbulent flows. *Phys. Fluids* **26** (8), 2088–2097.

KIM, J. 1989 On the structure of pressure fluctuations in simulated turbulent channel flow. *J. Fluid. Mech.* **205**, 421.

KIM, J., CHOI, J. & SUNG, H. J. 2002 Relationship between wall-pressure fluctuations and streamwise vortices in a turbulent boundary layer. *Phys. Fluids* **14** (2), 898–901.

KIM, J., MOIN, P. & MOSER, R. 1987 Turbulence statistics in fully developed channel flow at low Reynolds number. *J. Fluid Mech.* **177**, 133–166.

KLEWICKI, J. C. & HIRSCHI, C. R. 2004 Flow field properties local to near-wall shear layers in a low Reynolds number turbulent boundary layer. *Phys. Fluids* **16**, 4163–4176.

KOBASHI, Y. & ICHIJO, M. 1986 Wall pressure and its relation to turbulent structure of a boundary layer. *Exp. Fluids* **4**, 49.

KOSCHATZKY, V., MOORE, P. D., WESTERWEEL, J., SCARANO, F. & BOERSMA, B. J. 2011 High speed PIV applied to aerodynamic noise investigation. *Exp. Fluids* **50**, 863–876.

KROGSTAD, P.-Å. & ANTONIA, R. A. 1994 Structure of turbulent boundary layers in smooth and rough walls. *J. Fluid Mech.* **277**, 1–21.

LIU, X. & KATZ, J. 2006 Instantaneous pressure and material acceleration measurements using a four-exposure PIV system. *Exp. Fluids* **41**, 227–240.

LIU, Z. C., LANDRETH, C. C., ADRIAN, R. J. & HANRATTY, T. J. 1991 High resolution measurement of turbulent structure in a channel with particle image velocimetry. *Exp. Fluids* **10**, 301–312.

LUEPTOW, R. M. 1995 Transducer resolution and the turbulent wall pressure spectrum. *J. Acoust. Soc. Am.* **97**, 370–378.

MEINHART, C. D., WERELEY, S. T. & SANTIAGO, J. G. 2000 A PIV algorithm for estimating time-averaged velocity fields. *Trans. ASME: J. Fluids Engng* **122**, 285–289.

NA, Y. & MOIN, P. 1998 The structure of wall-pressure fluctuations in turbulent boundary layers with adverse pressure gradient and separation. *J. Fluid Mech.* **377**, 347–373.

NAGUIB, A. M., WARK, C. E. & JUCKENHÖFEL, O. 2001 Stochastic estimation and flow sources associated with surface pressure events in a turbulent boundary layer. *Phys. Fluids* **13** (9), 2611–2626.

NOVARA, M., IANIRO, A. & SCARANO, F. 2013 Adaptive interrogation for 3D-dimensional-PIV. *Meas. Sci. Technol.* **24**, 024012.

PERRY, A. E, HENBEST, S. & CHONG, M. S. 1986 A theoretical and experimental study of wall turbulence. *J. Fluid Mech.* **165**, 163–199.

POPE, S. B. 2000 *Turbulent Flows*. Cambridge University Press.

RATHNASINGHAM, R. & BREUER, K. S. 2003 Active control of turbulent boundary layers. *J. Fluid Mech.* **495**, 209.

ROBINSON, S. K. 1990 A perspective on coherent structures and conceptual models for turbulent boundary layer physics. *AIAA Paper* 90-1638.

ROBINSON, S. K. 1991 Coherent motions in the turbulent boundary layer. *Annu. Rev. Fluid Mech.* **23**, 601–636.

SCARANO, F. & POELMA, C. 2009 Three-dimensional vorticity patterns of cylinder wakes. *Exp. Fluids* **47**, 69–83.

SCHEWE, G. 1983 On the structure and resolution of wall-pressure fluctuations associated with turbulent boundary-layer flow. *J. Fluid Mech.* **134**, 311.

SCHRÖDER, A., GEISLER, R., ELSINGA, G. E., SCARANO, F. & DIERKSHEIDE, U. 2008 Investigation of a turbulent spot and tripped turbulent boundary layer flow using time-resolved tomographic PIV. *Exp. Fluids* **44**, 305–316.

SHAW, R. 1960 Influence of hole dimensions on static pressure measurements. *J. Fluid Mech.* **7**, 550–564.

SHENG, J., MALKIEL, E. & KATZ, J. 2009 Buffer layer structures associated with extreme wall stress events in a smooth wall turbulent boundary layer. *J. Fluid Mech.* **633**, 17–60.

SMITH, C. R. & METZLER, S. P. 1983 The characteristics of low-speed streaks in the near-wall region of a turbulent boundary layer. *J. Fluid Mech.* **129**, 27–54.

SPALART, P. R. 1988 Direct simulation of a turbulent boundary layer up to $Re_\theta = 1400$. *J. Fluid Mech.* **187**, 61–89.

STANISLAS, M., PERRET, L. & FOUCAUT, J. M. 2008 Vortical structures in the turbulent boundary layer: a possible route to a universal representation. *J. Fluid Mech.* **602**, 327.

THEUNISSEN, R., SCARANO, F. & REITHMULLER, M. L. 2008 On improvement of PIV interrogation near stationary interfaces. *Exp. Fluids* **45**, 557–572.

THOMAS, A. S. W. & BULL, M. K. 1983 On the role of wall-pressure fluctuations in deterministic motions in the turbulent boundary layer. *J. Fluid Mech.* **128**, 283.

TOWNSEND, A. 1976 *The Structure of Turbulent Shear Flow*, 2nd edn. Cambridge University Press.

TSUJI, Y., FRANSSON, J. H. M., ALFREDSSON, P. H. & JOHANSSON, A. V. 2007 Pressure statistics and their scaling in high-Reynolds-number turbulent boundary layers. *J. Fluid Mech.* **585**, 1–40.

VEDULA, P. & YEUNG, P. K. 1999 Similarity scaling of acceleration and pressure statistics in numerical simulations of isotropic turbulence. *Phys. Fluids* **11**, 1208–1220.

VIOLATO, D., MOORE, P. & SCARANO, F. 2011 Lagrangian and Eulerian pressure field evaluation of rod-aerofoil flow from time-resolved tomographic PIV. *Exp. Fluids* **50**, 1057–1070.

WESTERWEEL, J. 1997 Fundamentals of digital particle image velocimetry. *Meas. Sci. Technol.* **8**, 1379–1392.

WIENEKE, B. 2008 Volume self-calibration for three-dimensional particle image velocimetry. *Exp. Fluids* **45**, 549–556.

WILLMARTH, W. W. 1975 Pressure fluctuations beneath turbulent boundary layers. *Annu. Rev. Fluid Mech.* **7**, 13.

WILLMARTH, W. W. & WOOLDRIDGE, C. E. 1962 Measurements of the fluctuating pressure at the wall beneath a thick turbulent boundary layer. *J. Fluid Mech.* **14**, 187.